Pressurized Chemical Looping Combustion of Natural Gas with Ilmenite for SAGD Application: An Oxidation Kinetic Study and Preliminary Air Reactor Model

By
Shazadi Rana

Thesis submitted in partial fulfillment of the requirements for the
Master of Applied Science degree in Chemical Engineering

Department of Chemical and Biological Engineering
University of Ottawa
May 2018

Abstract

To prevent the global surface temperature from increasing past the 2 ^{o}C target, it is necessary to address CO_2 emissions from small point sources. Within Canada's heavy oil industry, SAGD facilities use natural gas combustion to produce the large amounts of steam required for the process, which produces approximately 0.5-2 Mtonnes of CO_2 per annum. A suitable technology for CO_2 mitigation from a SAGD facility is Pressurized Chemical Looping Combustion. PCLC is an oxy-combustion, carbon capture technology with a relatively low predicted energy penalty of 3-4%. The process requires a dual, interconnected fluidized bed reactor system with circulating solids. Natural gas is converted in the fuel reactor via a solid metal oxide, which is then circulated to the air reactor for reoxidation with air. As the cost of air compression is significant, the economical feasibility of the process is reliant on air reactor performance. The objective of this study is to investigate the oxidation reaction and derive a kinetic model for reactor design and performance assessment purposes.

Ilmenite ore was chosen as the metal oxide, as it is low cost and has desirable oxygen transport properties for PCLC. Pressurized TGA tests were conducted to study the effects of oxygen concentration, temperature and pressure on the rate of the oxidation reaction. The total pressure was varied from 1-16 bara at 900 ^{o}C with air. The oxygen concentration was varied from 2.5-21 vol%, and the temperature from 800-1000 ^{o}C at 8 bar.

Temperatures below 850 ^{o}C resulted in segregation of the Fe and Ti phase in the ilmenite ore, leading to a reduction in the overall oxygen carrying capacity. Crack formation was observed at higher oxygen partial pressures, resulting in increased surface area for reaction and a fast reaction rate. At lower oxygen partial pressures, a solid-state diffusion controlled regime was observed due to the absence of fissures.

A dual mechanistic oxidation kinetic model was derived at 8 bar, with 2nd order random nucleation dominating at lower conversions, and Jander's solid state diffusion model dominating at higher conversions. The transition from the nucleation and growth to the

diffusion-controlled portion occurred at higher conversions with higher oxygen partial pressure. The activation energy was 16.6 kJ/mol and 48.7 kJ/mol while the order of reaction with respect to oxygen was 0.3 and 1.3 for respectively the nucleation and growth, and diffusion-controlled regimes. A preliminary air reactor model is constructed as a turbulent bed. The turbulent bed is modelled as an axial dispersion reactor for a basic performance assessment.

Sommaire

Pour éviter que la température de surface globale ne dépasse la cible de 2 °C, il est nécessaire de traiter les émissions de CO_2 provenant de petites sources ponctuelles. Au sein de l'industrie canadienne du pétrole lourd, les installations de « Steam Assisted Gravity Drainage » SAGD utilisent la combustion de gaz naturel pour produire les grandes quantités de vapeur d'eau nécessaires au procédé, qui produit environ 0,5 à 2 Mt de CO_2 par année. Une technologie appropriée pour l'atténuation du CO_2 à partir d'une installation SAGD est la combustion en boucle chimique pressurisée. PCLC est une technologie de capture du carbone par oxy-combustion avec une pénalité d'énergie prédite relativement faible de 3 à 4%. Le procédé nécessite un double système de réacteur à lit fluidisé interconnecté avec des solides en circulation. Le gaz naturel est converti dans le réacteur à combustible par l'intermédiaire d'un oxyde métallique solide, qui est ensuite mis en circulation dans le réacteur à air pour être réoxydé par l'air. Comme le coût de la compression de l'air est important, la faisabilité économique du procédé dépend du rendement du réacteur. L'object de cette étude est d'enquêter sur la réaction d'oxydation et dériver un modèle cinétique pour la conception du réacteur et l'évaluation des performances.

Le minerai d'ilménite a été choisi comme oxyde métallique, car il est peu coûteux et possède des propriétés de transport de l'oxygène souhaitables pour PCLC. Des tests thermogravaires (TGA) sous pression ont été effectués pour étudier les effets de la concentration en oxygène, de la température et de la pression sur la vitesse de la réaction d'oxydation. La pression totale varie de 1 à 16 bara à 900 °C avec de l'air. La concentration d'oxygène a varié de 2,5 à 21% en volume et la température de 800 à 1000 °C à 8 bar.

Des températures inférieures à 850 °C ont entraîné une ségrégation de la phase Fe et Ti dans le minerai d'ilménite, entraînant une réduction de la capacité globale de transport d'oxygène. La formation de fissures a été observée à des pressions partielles plus élevées en oxygène, ce qui a entraîné une augmentation de la surface de réaction et une vitesse de réaction

rapide. À des pressions partielles inférieures d'oxygène, un régime contrôlé de diffusion à l'état solide a été observé en raison de l'absence de fissures.

Un modèle cinétique d'oxydation double mécanisme a été dérivé à 8 bar, avec une nucléation aléatoire de second ordre dominant à des conversions plus faibles, et le modèle de diffusion à l'état solide de Jander dominant aux conversions plus élevées. La transition de la partie de nucléation et de croissance à la partie contrôlée par diffusion s'est produite à des conversions plus élevées avec une pression partielle d'oxygène plus élevée. L'énergie d'activation était de 16,6 kJ / mol et de 48,7 kJ / mol tandis que l'ordre de réaction vis-à-vis de l'oxygène était de 0,3 et de 1,3 pour respectivement les régimes de nucléation et de croissance et de diffusion contrôlée. Un modèle préliminaire de réacteur à air est construit sous la forme d'un lit turbulent. Le lit turbulent est modélisé comme un réacteur à dispersion axiale pour une évaluation de performance de base.

Acknowledgements

First and foremost, I would like to thank God Almighty for giving me the opportunity, ability and strength to complete this research study.

I would like to express my sincere gratitude to my co-supervisors, Dr. Arturo Macchi and Dr. Poupak Mehrani. Without their guidance and support, this work would not have been possible. I owe a considerable amount of personal and professional development to them.

I would like to thank the entire Fluidized Bed Combustion and Gasification team at CanmetENERGY for their technical advice and assistance during my graduate studies. I would like to thank Dr. Zhenkun Sun for the considerable amount of support with the particle characterization work. I would like to thank Dr. Yewen Tan for his perseverance in troubleshooting the PTGA on many occasions. I would like to thank Dr. Marc Duchesne and Robert Symonds for their frequent advice and support. I would like to thank Dr. Robin Hughes and Dennis Lu for their oversight during my stay.

Lastly, I would like to thank my family and friends for their love and encouragement. All that is good in me is a reflection of them.

Statement of Contribution of Collaborators

I am the sole author of all the chapters of this thesis. My supervisors, Dr. Arturo Macchi and Dr. Poupak Mehrani of the Department of Chemical and Biological Engineering and Dr. Robin Hughes and Dr. Zhenkun Sun of CanmetENERGY supervised my work during the M.A.Sc program and provided editorial corrections.

Signature: _____ Date: _____

Acronyms

ADR	Axial Dispersion Reactor
CCS	Carbon Capture and Storage
GHG	Greenhouse Gas
IROC	Instantaneous Rate of Change
LHV	Lower Heating Value
NGCC	Natural Gas Combined Cycle
OC	Oxygen Carrier
OTSG	Once-Through Steam Generator
PCLC	Pressurized Chemical Looping Combustion
SAGD	Steam Assisted Gravity Drainage
TGA	Thermogravimetric Analyzer

Nomenclature

Ar	Archimedes number, (=$\rho_g(\rho_p - \rho_g)gd_p^3/\mu^2$) [-]
C_i	Concentration of species i [mol/m^3]
d	Reactor/Bed Diameter [m]
l	Reactor/Bed Length [m]
m_{ox}	Mass in oxidized state [mg]
m_{red}	Mass in reduced state [mg]
Mm_i	Molar Mass of Species i [g/mol]
P	Pressure [Pa]
Pe	Peclet number [-]
r_i	Rate of reaction with respect to i [mol/m^3.s]
R_{oc}	Oxygen Carrying Capacity [wt%]
Re	Reynolds Number (=$\rho_g U d_p/\mu$) [-]
Sc	Schmidt Number (=$\mu/\rho_g d$) [-]
T	Temperature [K]
t	Time [s]
U	Superficial Gas Velocity [m/s]
v_p	Particle Velocity [m/s]
$y_{AM/CR}$	Mass Fraction present as the Amorphous phase or crystalline phase [wt%]
X	Conversion [-]
x_i	Mass Fraction of Species i [wt%]

ϵ	Bed Voidage [-]
ϵ_s	Solids Hold-up [-]
τ_i	Rate Constant or Time for complete solid conversion [s]
τ_i'	Lumped Kinetic Constant
ρ_g	Gas Density [kg/m^3]
ρ_p	Particle Density [kg/m^3]
μ	Gas Viscosity [Pa.s]

Table of Contents

List of Tables

List of Figures

Chapter 1 -Introduction

1.1 Global Warming and CLC

The global surface temperature has been increasing steadily, with the past 16 years ranking among the top 17 warmest since 1850 [1]. A temperature increase greater than 2 ^{o}C above pre-industrial level is predicted to have dire consequences on ecology and wild life [2]. The scientific community is of the consensus that climate change is the direct results of increased greenhouse gas (GHG) emissions due to industrialization. As human activity is the likely cause of global warming, the resulting catastrophic weather patterns can be prevented by a proactive stance towards the reduction of GHGs emitted to the atmosphere. CO_2 is the most abundant of GHGs, with the longest lifetime and a high potency in regards to heat trapping. CO_2 accounts for 91% of total CO_2 equivalent GHG emissions [3]. The Paris agreement was established in 2015 as an international effort towards CO_2 mitigation, with Canada pledging to cut emissions to 30% below 2005 levels by 2030 [4].

Anthropogenic CO_2 emission from fossil fuel combustion account 65% of global CO_2 emissions [5]. Despite the predicted increase in renewable energy sources, fossil fuels will continue to dominate the global energy market in the near future. Global fossil fuel demand is estimated to continue to rise in subsequent years and plateau by 2030 [6]. Hence the development and implementation of Carbon Capture and Storage (CCS) technologies is crucial in mitigating CO_2 emissions.

Of the carbon capture technologies under consideration, amine scrubbing and oxyfuel combustion are the most developed. The energy penalty associated with amine scrubbing is approximately 12% and oxyfuel combustion is 10% [7], which makes them unappealing to industry. Chemical Looping Combustion (CLC) is a novel oxy-combustion technology with a lower penalty of 3-4%, as well as a high capture efficiency. The system consists of a dual, interconnected fluidized bed reactor system as seen in Figure 1-1. Fuel is converted in the fuel reactor via a solid metal oxide, which is then circulated to the air reactor to be re-oxidized. Since there is in principle no contact between the air and fuel, the CO_2 stream produced remains undiluted with N_2, avoiding the costly air separation step.

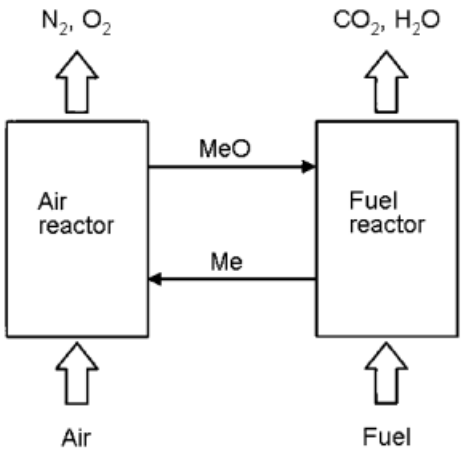

Figure 1-1: Dual Interconnected Fluidized Bed Reactor System in CLC [8]

Due to the improved electric efficiencies offered by a natural gas combined cycle (NGCC), CLC must be pressurized to compete with post-combustion scrubbing on a NGCC [9], [10]. Pressurized operation allows for power recovery through gas turbine technology from the air reactor, as well as reduces downstream power requirements for CO_2 compression. A

greater amount of fuel can also be processed in a lesser volume with pressurized operation, which is beneficial for implementation in remote locations.

Pressurized CLC is potentially a suitable carbon capture technology for steam production via natural gas combustion for steam-assisted gravity drainage (SAGD). As more than 85% of Canada's oil sands are accessible through in-situ technologies such as SAGD, the steam demand in the heavy oil industry is projected to increase. Currently in SAGD facilities, once-through steam generators (OTSGs) are employed for steam production using natural gas combustion. Each OTSG produces approximately 125 ton/hr of steam and emits 64 ton/hr CO_2 [11]. Through the replacement of OTSGs with chemical looping combustion system, the 0.5-2 Mtonnes of CO_2 per annum currently emitted by a typical in-situ bitumen production facility can be mitigated, bringing Canada closer to its carbon capture target.

1.2 Ilmenite as Oxygen Carrier

In selecting an oxygen carrier, considerations are given to the oxygen carrying capacity, reactivity for reduction and oxidation reactions, mechanical stability, fluidizing capabilities (low agglomeration), environmental impact and cost. Copper, Nickel, Iron and Manganese based metal oxides have been extensively studied for CLC application[12], [13]. Most of these oxygen carriers require support material to enhance reactivity, oxygen transport capacity and/or mechanical integrity, which significantly adds to their production cost. Natural ilmenite ore is a low cost, iron-titanium based oxygen carrier suitable for CLC. Canada is the fourth largest producer of ilmenite, with the majority of the reserves located

in northern Quebec [14]. Although the titanium in the ore does not supply oxygen to the fuel, the presence of titanium in the ore improves the oxygen transfer capabilities of iron. The addition of inert metal oxides has proven to increase the sintering temperature, enhance the reactivity through the formation of a more porous structure and in the case of Fe based oxygen carriers, increase the oxygen transport capacity by allowing Fe to reduce to lower oxidation states [15].

In the oxidized state, ilmenite ore mainly consists of pseudobrookite (Fe_2TiO_5), rutile (TiO_2) and hematite (Fe_2O_3), which are reduced to ilmenite ($FeTiO_3$) and Magnetite (Fe_3O_4), as shown in Equations 3 and 4,. Although it is possible for Fe_3O_4 to reach lower oxidation states (e.g. FeO/elemental Fe), this is unfavorable in CLC with natural gas due to the associated thermodynamic limitations resulting in the formation of partial combustion products and syngas generation. FeO and Fe also tend to agglomerate at relatively low temperatures. The oxidation reaction of ilmenite is highly exothermic, with an enthalpy of 470 kJ/mol O_2 [16], and localized heating of the particle along with the high operating temperature (>900 ^oC) necessary for the process may pose a problem with agglomeration in the presence of FeO and Fe. Reduction of the oxygen carrier below Fe_3O_4 is prevented with the presence of CO_2 in the gaseous mixture.

Ilmenite has been extensively studied for atmospheric pressure CLC. Kinetic models have been developed for the cyclic redox reaction under atmospheric pressure, with the focus being on the reduction reaction [17], [18] since the oxidation kinetics are relatively fast and air, the oxidizing gas, is abundantly available. Pilot scale demonstrations using ilmenite have

also been conducted on units up to 120 kWth with natural gas and 1 MWth with coal as the fuel [19]–[24]. A limited number of studies have been done under pressurized conditions. Tan et al. studied the reduction kinetics of ilmenite with CH_4 at 9 and 16 bar [25] and Lu et al. investigated the effect of pressure up to 24 bar on the reduction reaction with CO [26]. However studies on the oxidation reaction at high pressure are lacking.

The effect of pressure on gas-solid reaction kinetics has been polarizing in literature. Abad et al. found pressure in the range of 1-30 bar to hinder both the oxidation and reduction kinetics with Copper, Iron and Nickel based oxygen carriers while maintaining a constant gas mole fraction, indicating that the negative effect of pressure exceeds the positive effect of increased reacting gas partial pressure. The conclusion drawn was to derive a kinetic model specific to the operating pressure of the reactor system, due to insufficient model fits [27]. Nordes et al. used a fixed bed to test Ni and Cu based oxygen carriers at a pressure range of 1-10 bar and also found the redox kinetics to decrease with increased pressure while maintaining the same mole fraction [28]. Testing pressures up to 10 atm, Desphande et al. found the pressure to have a negative effect on the redox kinetics with a constant reacting gas partial pressure, and a positive effect with a constant reacting gas mole fraction using an iron-titanium complex [29]. Jin and Ishida found the pressure to have a negative effect on the reduction reaction using a Nickel based oxygen carrier with natural gas at pressures between 1-3 atm in a fixed bed reactor, with a constant methane volume fraction[30]. Hamers et al studied the redox reaction of Cu and Ni based oxygen carrier in a TGA at pressures of 1-30 bar with CO and H_2 , and found pressure to negatively impact kinetics with a constant reacting gas partial pressure[31]. Hamers et al also tested $NiO/CaAl_2O_3$ as an

oxygen carrier with H_2 and syngas in a packed bed reactor at a pressure of 2 to 7.5 bar while maintaining a constant gas composition, and found pressure had minimal effect on the reaction conversion for both oxidation and reduction [32]. San Pio et al. reported no correlation between pressure and reduction reaction rate when testing pressures up to 8 bar, and attributed the negative pressure effects found in previous studies to external mass transfer limitations [33]. Xiao et al constructed a pilot-scale coal-fueled PCLC unit to study the performance of iron ore as oxygen carrier, and found higher operating pressure to increase overall fuel conversion in the range of 1-5 bar[34].

The oxidation of the ilmenite species is a complex multi-step and multi-pathway reaction, which can result in various products depending on the reacting time and temperature. According to Xiao et al., the oxidation products below 800 ^{o}C are rutile, hematite and a metastable compound pseudorutile ($Fe_2Ti_3O_9$) formed by parallel reaction pathways shown in equations 1a and 2a. Above 900 ^{o}C, pseudobrookite and rutile are the stable products, generated through equations 1b and 2b. With an insufficient reacting time or temperature below 900 ^{o}C, the oxidation reaction does not reach completion and the intermediary products are favored [35]–[37].

$$4FeTiO_3 + O_2 \rightarrow 2Fe_2O_3 + 4TiO_2 \quad (1a)$$

$$Fe_2O_3 + TiO_2 \rightarrow Fe_2TiO_5 \quad (1b)$$

$$12FeTiO_3 + 3O_2 \rightarrow 4Fe_2Ti_3O_9 + 2Fe_2O_3 \quad (2a)$$

$$2Fe_2Ti_3O_9 + Fe_2O_3 \rightarrow 3Fe_2TiO_5 + 3TiO_2 \quad (2b)$$

The overall oxidation reactions in the ilmenite ore can be simply stated by the following expressions:

$$4FeTiO_3 + O_2 \rightarrow 2Fe_2TiO_5 + 2TiO_2 \quad (3)$$

$$4Fe_3O_4 + O_2 \rightarrow 6Fe_2O_3 \quad (4)$$

Since the reduction of hematite is possible down to Fe_3O_4, only a third of the Fe^{3+} from hematite can be reduced Fe^{2+} whereas two-thirds remains as Fe^{3+}. All the Fe^{3+} from the pseudobrookite phase is reduced to Fe^{2+} as the ilmenite phase, hence iron present in pseudobrookite offers a higher oxygen carrying capacity compared with iron in the hematite phase. The mass change from reducing pseudobrookite to ilmenite is 5%, whereas from hematite to magnetite is 3.3%. The higher the fraction of ilmenite in the ore, the larger the overall carrying capacity is expected to be.

1.3 Thesis Objective

The oxidation reaction of ilmenite under pressurized conditions is an essential knowledge gap in process design and analysis, as process economics are highly dependent on the air reactor performance. Cost optimization of PCLC for steam production requires a trade-off between air reactor bed inventory and the extent of oxygen uptake by the oxygen carrier from the compressed inlet air stream. Therefore, this study aims to develop a kinetic model for ilmenite's oxidation at increased pressure to integrate into PCLC reactor model.

Chapters 2 and 3 are focused on the derivation of an oxidation kinetic model for PCLC. Chapter 2 describes the experimental technique and equipment used to study the kinetic parameters. A schematic and description of the pressurized TGA, a summary of the test matrix and the method of data analysis are detailed in this chapter. Chapter 3 presents the experimental results, and the kinetic model for the oxidation reaction. The effect of temperature, oxygen partial pressure and total pressure (with both a constant O_2 mole fraction and constant O_2 partial pressure) are presented in this chapter. Chapter 4 contains a preliminary air reactor model, designed as a turbulent bed, and a brief performance assessment. Lastly, Chapter 5 presents concluding remarks and recommendations for future work.

Chapter 2 -Materials and Methods

2.1 Experimental Set-up

The Ilmenite used in this study was supplied by Rio Tinto as a beneficiated rock. The mined ore had been processed by the manufacturer to remove the gangue material and produce a finer concentrate. The ilmenite was crushed, sieved and calcined for 2 hours in a muffle furnace at 900 ^{o}C in air. The composition of the calcined ilmenite was determined from XRD and XRF analysis, shown in Table 2-2. Particle diameter of 106-212 um was used, as this particle size falls in the range giving the desired fluidization behaviour for the reactor system. Also, previous studies show no effect of particle diameter in the range of 45-300 um on the reduction reaction kinetics with this particular ilmenite [25]. The characteristics and reduction kinetics of this ilmenite have been previously studied with CO, H_2 and CH_4. The results showed reasonable reactivity with the reducing gases and desirable oxygen transport properties for CLC [25], [26], [38]. The ilmenite ore was also successfully tested as bed material in an oxy- fluidized bed combustor (oxy-FBC) to enhance fuel conversion by supplying oxygen in localized oxygen deficient regions [39].

Linseis's STA HP/2 pressurized thermogravimetric analyzer was used to perform consecutive redox cycles. The schematic of the equipment is shown in Figure 2-1. As the process is designed with a CO_2 recycle making up 50% of the fuel reactor inlet gas, the reducing gas mixture was maintained at ratios of 1:2:1 for CH_4:CO_2: H_2O, to simulate an average of the fuel reactor inlet and outlet conditions. The CO_2 prevents thermal

decomposition of methane occurring at high temperatures, as well as reduction below magnetite.

Although a high operating pressure is predicted to have a higher process efficiency, there is an upper pressure limit to the efficiency gain where the power requirement for the air compressor exceeds the additional power recovery from the gas turbine in the combined cycle. Considering overall fuel efficiency of the process, the optimal operating pressure range is 5-10 bar[10]. The average of this range was chosen to represent high pressure kinetics in PCLC and the oxidation kinetic model was derived for 8 bar.

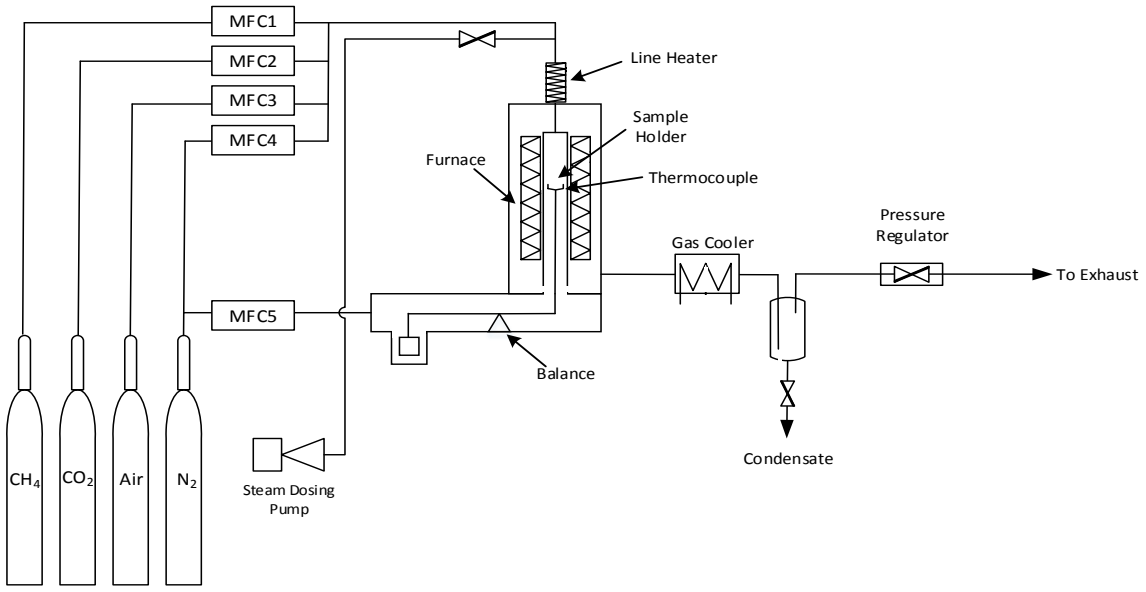

Figure 2-1: Schematic of Pressurized Thermogravimetric Analyzer

The reducing gas was composed of 15 vol% CH_4, with CO_2 and H_2O in the desired proportions and nitrogen to balance. The temperature during the reduction cycles was maintained at 900 ^oC. The oxidation temperature was varied from 800 ^oC-1000 ^oC. The optimal air reactor

temperature is at the upper end of the tested range whereas the lower temperatures are tested for scientific curiosity. Air was diluted with nitrogen to simulate vitiated air in the reactor system. Oxygen partial pressures from 0.2-1.68 bar were tested, corresponding to an oxidizing gas composition of 2.5-21 vol% oxygen at a total pressure of 8 bar. The pressure was also varied from 1-16 bar at 900 ^{o}C using air as the oxidizing gas. Nitrogen is used to purge the reaction chamber between each oxidation and reduction cycle. The oxidation, reduction and nitrogen purge cycles were 7, 10 and 2.5 minutes respectively. As the ilmenite particles undergo an activation period of several cycles after which the reactivity stabilizes, the 10th cycle oxidation was used to model the kinetics. Figure 2-2 shows the increase and subsequent stabilization of reactivity of ilmenite over the 10 cycles. Througout the activation process, the surface morphology of the particles change, as seen in the SEM images in Figure 2-3. N_2 adsorption-desorption analysis of the calcined particle and particles in the oxidized state having undergone 8 redox cycles at atmospheric pressure show a BET specific surface area increase from 0.10 to 0.53 m^2/g, as presented in Table 2-1.

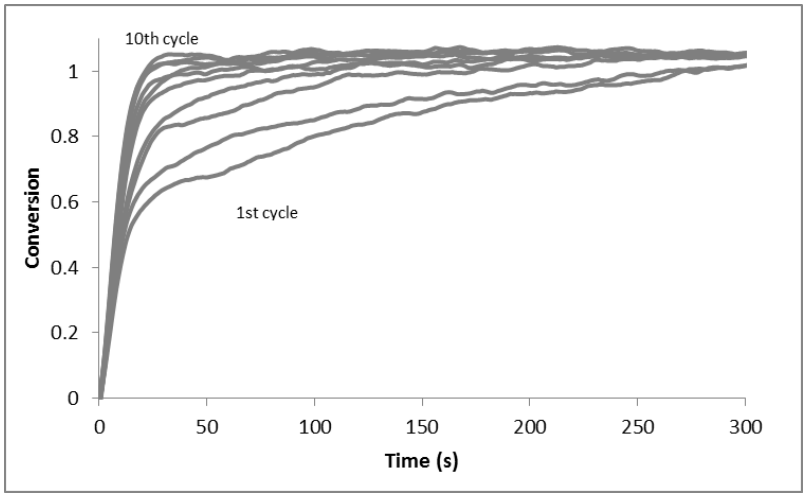

Figure 2-2: Ilmenite Activation over 10 oxidation cycles. Test conditions: Total $\boldsymbol{P}$=8 bar, $\boldsymbol{T}$=900 ^{o}C, $\boldsymbol{Pp_{O_2}}$=1.68 bar.

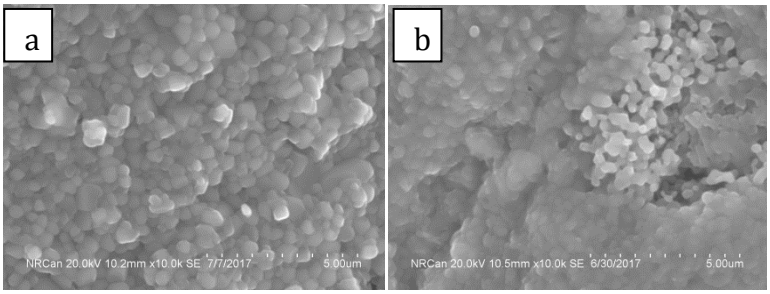

Figure 2-3: SEM images of ilmenite after a) calcination b) 10 redox cycles at 8 bar (in the oxidized state)

Table 2-1: Physical properties of raw, calcined and 8th cycle oxidized particles under atmospheric pressure from BET and BJH analysis.

	Raw	**Calcined**	**8th cycle Oxidized**
Specific Surface Area (m^2/g)	0.13	0.10	0.53
Specific Pore Volume (cm^3/g)	$0.2x10^{-4}$	$4.3x10^{-4}$	$15.3x10^{-4}$
Mean Pore Size (nm)	30.9	30.0	13.5

Preliminary tests were conducted to ensure gas film mass transfer or inter-particle diffusion did not affect the reaction rates. At a pressure of 8 bar, the gas flowrate was varied from 1 to 3 NL/min and the sample loading from 20 mg to 100 mg. As there was no effect of gas flowrate and sample size on the reaction rate at 2NL/min and 40 mg, the PTGA experiments at 8 bar were conducted at these conditions. For the experiments with varying pressure, the gas flowrate was varied in proportion to the pressure to maintain a constant space velocity. The preliminary tests are further detailed in Appendix A3.

2.2 Data Evaluation

The oxygen carrying capacity (R_o) is defined as the ratio of mass change between redox states to the mass in the oxidized state. The overall carrying capacity of ilmenite is the sum of the contribution from Fe_2TiO_5 and Fe_2O_3. XRD analysis was used to determine the composition of the individual compounds in the crystalline phase, as well as the overall mass fraction present as the crystalline phase. XRF analysis was used to determine the total Fe, Ti and O composition in both the crystalline and amorphous phases. The XRF results present all iron as Fe_2O_3 and all titanium as TiO_2. The results from the XRD and XRF were consolidated to determine the overall composition of the calcined ilmenite ore as show in Table 2-2 below. Calcination brings all oxide species to their most oxidized state, hence only Fe_2TiO_5, Fe_2O_3 and TiO_2 are present in the calcined particles. Further details on the calculations are provided in the appendices.

Table 2-2: Calcined ilmenite composition based on XRD and XRF Analysis

	XRD	XRF	Consolidated
Composition (wt%)			
Pseudobrookite (Fe_2TiO_5)	46.6		49.9
Hematite (Fe_2O_3)	27.0	60.9	28.7
Rutile (TiO_2)	4.0	36.5	18.8
Inert		2.6	2.6
Crystallinity (wt%)	77.5		

The mass fraction of each species in calcined ilmenite along with their respective oxygen carrying capacity are used to calculate a theoretical carrying capacity of 4.3%. Hence the PTGA data was normalized with R_o of 4.3% to determine the conversion (X).

$$R_o = \frac{m_{ox} - m_{red}}{m_{ox}} \quad (5)$$

$$X = \frac{m - m_{red}}{R_o m_{ox}} \quad (6)$$

The Hancock and Sharp Method of solid-state kinetic data analysis was used to determine the rate controlling mechanism and the associated mechanistic rate law to model the oxidation reaction. The conversion of a gas-solid reaction can be represented by Equation 7, which can be linearized to give the Avrami-Erofeeve expression, as shown by Equation 8. The plot of ln[-ln(*1-X*)] vs ln*t*, also referred to as an Avrami-Erofeeve plot, is used to obtain the slope *m*, the value of which is indicative of the rate controlling mechanism. The corresponding mechanistic rate expression associated with different values of m are shown in Table 2-3.

$$X = 1 - e^{-kt^m} \quad (7)$$

$$\ln(-\ln\ (1 - X)) = m \ln t + \ln k. \quad (8)$$

The Avrami-Erofeev equation above is a generalized equation to represent solid-state reaction kinetics. The kinetic equations are classified into three categories based on the rate controlling mechanism. The solid-state diffusion (D) models consider diffusion through the crystal lattice of the product layer to be the rate limiting step. This group of models demonstrates a deceleratory behaviour, because of the decrease in rate with the growth of

the product layer, resulting from the lengthened pathway for diffusion. The geometric contraction (R) models are also a group of deceleratory models that assume the nucleation occurs very rapidly on the surface, and the rate is controlled by the progress of the reaction interface towards the center of the solid. The nucleation and growth or Avrami (A) models assume the formation and growth of nuclei govern the reaction kinetics. These models are characterized by the sigmoidal shape of the conversion vs time plots. The kinetics of the Avrami models experience an acceleratory portion in which the formation and growth of nuclei becomes rapid. As the reactants are consumed, the nucleation sites become saturated and the growing nuclei begin to coalesce together and ingest smaller nucleation sites, leading to a deceleratory rate[40]. A high level of experimental accuracy is required to differentiate between models in a group, as the difference between the associated Avrami-Erofeev constants for certain rate expressions are minor, as shown in Table 2-3.

The applicable rate expressions from the mechanistic group were evaluated by fitting experimental data, and the expression which provided the best fit based on the regression analysis was ultimately chosen to model the kinetics. The generalized reaction kinetics can be represented by Equation 9 below, with the mechanism associated rate expressions for $f(x)$ given in Table 2-3.

$$f(x) = \frac{t}{\tau_i} \tag{9}$$

For unchanging reaction conditions, the value of τ_i represents the time required for the solid reactant to reach full conversion. τ_i depends on physical parameters (geometry and morphology of solids), the model of transformation and reaction conditions. After determining the model of transformation (the reaction mechanism), τ_i is determined for

each experimental condition, and is further broken down to isolate for reaction conditions. The temperature and reacting gas concentration dependent terms are isolated as seen in Equation 10. τ_i ′ is the lumped constant for the oxidation kinetics incorporating the intrinsic properties which are assumed to be unchanging.

$$\tau_i = \frac{\tau_i{}'}{{C_g}^n e^{\left(-\frac{E_a}{RT}\right)}} \tag{10}$$

Under isothermal condition, the derived form of the rate expression is also useful in analysing the instantaneous rate of change (IROC).

$$\frac{dX}{dt} = \frac{1}{\tau_i} g(x) \tag{11}$$

The effect of oxygen partial pressure on the reaction rate was quantified by deriving the order of reaction with respect to oxygen. The effect of temperature was also quantified by generating an Arrhenius plot. These two parameters, along with the lumped constant formed the oxidation kinetic model.

Table 2-3: Slope of Avarami-Erofeev plots and corresponding solid-state kinetic rate expressions [41]

Kinetic Models	Rate Expression $f(x)$	Derived Form $g(x)$	Value of m
Solid-State Diffusion (D) Models			
D_1	X^2	$1/2X$	0.62
D_2	$(1-X)\ln(1-X)+X$	$1/[-\ln(1-X)]$	0.57
D_3	$\left[1-(1-X)^{\frac{1}{3}}\right]^2$	$(3/2)(1-X)^{2/3}[1-(1-X)^{1/3}]$	0.54
D_4	$1-\frac{2}{3}X-(1-X)^{2/3}$	$(3/2)[(1-X)^{-\frac{1}{3}}-1]$	0.57
Geometric Contraction (R) Models			
$Zero\ Order$	X	1	1.24
R_2	$1-(1-X)^{1/2}$	$2(1-X)^{1/2}$	1.11
R_3	$1-(1-X)^{1/3}$	$3(1-X)^{2/3}$	1.07
Nucleation and Growth (A) Models			
F_1	$-\ln(1-X)$	$(1-X)$	1.00
A_2	$[-\ln(1-X)]^{1/2}$	$2(1-X)[-ln(1-X)]^{1/2}$	2.00
A_3	$[-\ln(1-X)]^{1/3}$	$3(1-X)[-ln(1-X)]^{1/3}$	3.00

Chapter 3 -Results and Discussion

The oxidation reaction was relatively fast in air at 8 bar and 900 °C, reaching 50% conversion in approximately 10 seconds, and completion in less than 30 seconds. The conversion curve was observed to follow a sigmoidal shape, as seen in Figure 3-1. The instantaneous Rate of Change (IROC) was also plotted, to gain further insight into the reaction kinetics. As the sigmoidal shape and the significant portion of the IROC curve was unaltered by increasing the gas velocity, dispersion was eliminated as the cause, and the sigmoidal shaped was deemed characteristic of the oxidation kinetics. The observed shape is indicative of the nucleation and growth dominating as the rate controlling mechanism.

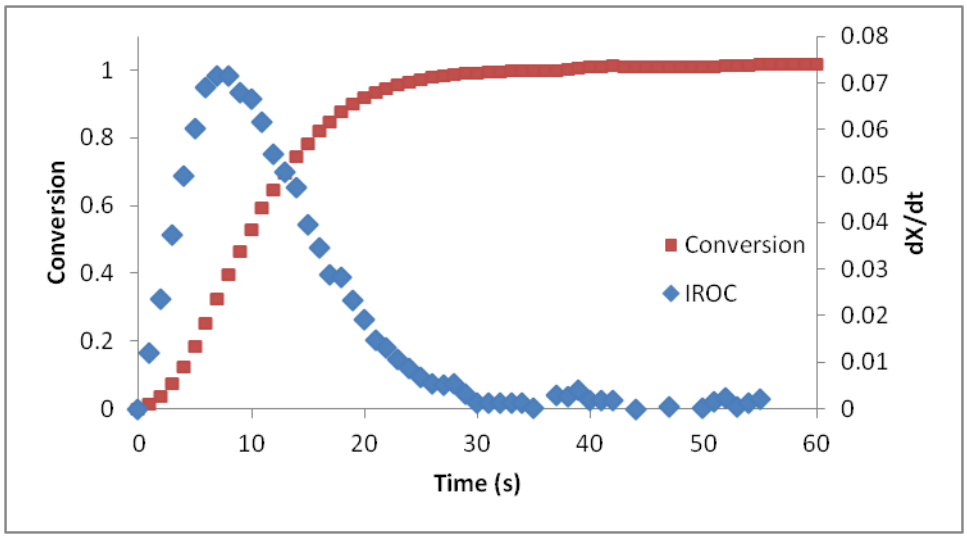

Figure 3-1: Oxidation conversion curve. Test conditions: Total P=8 bar, T=900 °C, Pp_{O_2}=1.68 bar.

3.1 Effect of Reducing Gas mixture on Oxidation

3.1.1 Methane Fraction

Under isothermal conditions, the thermodynamic driving force of a gas-solid chemical interaction is principally controlled by the gas composition[42]. Although the methane fraction in the experiments was based on an average in the fuel reactor, the solids will encounter a variety of reducing gas compositions. To ensure the chosen reduction mixture is representative of the PCLC system, and to assess the effects on the oxidation kinetics, the methane fraction in the reduction gas mixture was varied. Between 25 vol% and 15 vol% methane, while maintaining the same H_2O:CH_4:CO_2 ratio in the gas mixture, there was observed to be no difference in the oxidation kinetics.

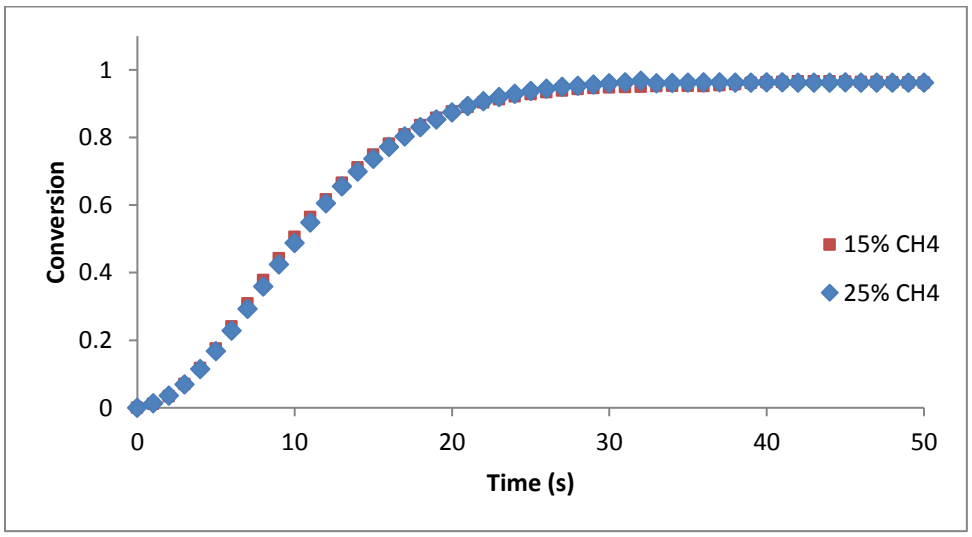

Figure 3-2: Effect of methane fraction in reducing gas mixture on oxidation kinetics. Test conditions: Total $\boldsymbol{P}$=8 bar, $\boldsymbol{T}$=900 °C, $\boldsymbol{Pp_{O_2}}$=1.68 bar.

3.1.2 Presence of Steam

The presence of steam with CO_2 and CH_4 in the reducing gas mixture is of interest, as these compounds will be present together in the fuel reactor. Abad et. al found the presence of steam to limit ilmenite's conversion when using H_2 as fuel. The increased conversion without steam was attributed to the reduction of Fe_3O_4 to FeO [43]. With natural gas as the fuel, the presence of CO_2 prevents reduction below Fe_3O_4. Tan et. al tested the use of steam in lieu of carbon dioxide on the reduction of ilmenite with methane, and stated there was no significant difference between the different product gases being present in the reduction mixture[25]. The presence of steam in addition to CO_2 on ilmenite's oxidation has not been reported at high pressures. Figure 3-3 highlights the effect of using steam in the reduction mixture, on the oxidation kinetics. The initial fast portion of the tests with steam and no steam overlap. There is a slightly more sloped latter portion where a higher rate of change is observed. Figure 3-4 shows the rate drops faster when steam was used. A slightly higher conversion is also reached without steam, which is possibly due to a small portion of Fe_3O_4 being converted FeO. FeO also has a higher tendency to agglomerate, hence the latter, solid-state diffusive portion of a TGA curve would be steeper without steam.

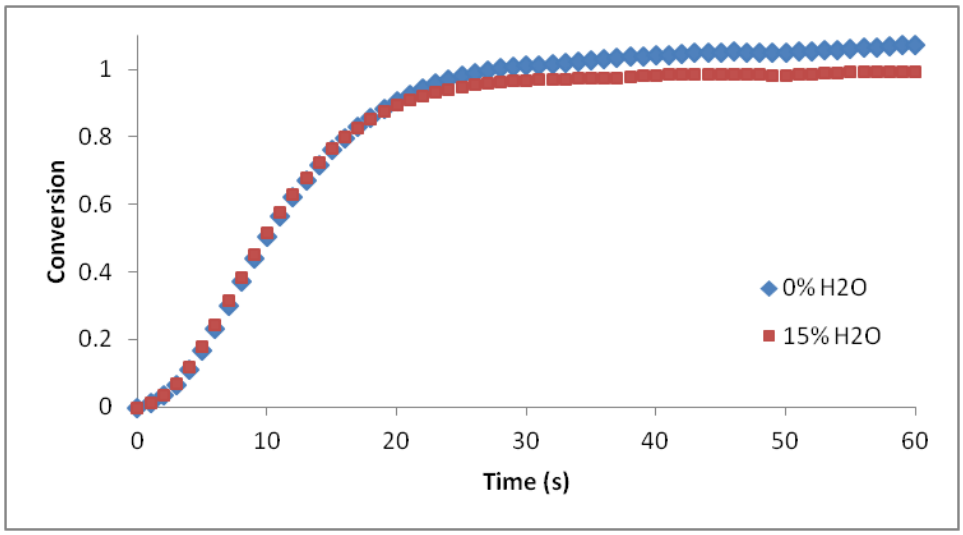

Figure 3-3: Oxidation kinetics with and without steam in reducing gas mixture. Test conditions: Total $\boldsymbol{P}$=8 bar, $\boldsymbol{T}$=900 °C, $\boldsymbol{Pp_{O_2}}$=1.68 bar.

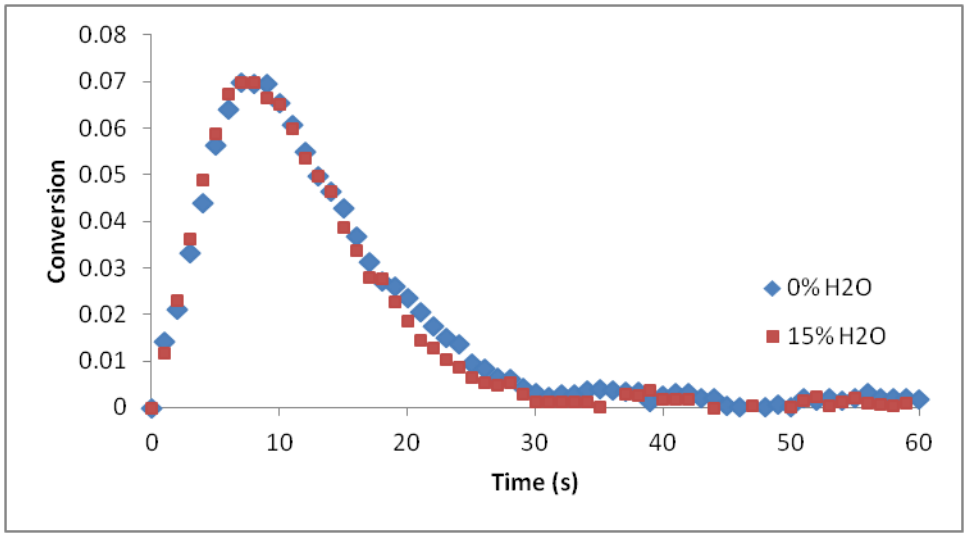

Figure 3-4: IROC of oxidation with and without steam in reducing gas mixture. Test conditions: Total $\boldsymbol{P}$=8 bar, $\boldsymbol{T}$=900 °C, $\boldsymbol{Pp_{O_2}}$=1.68 bar.

3.2 Effect of Oxygen Partial Pressure

Figure 3-5 shows the oxidation conversion vs. time curves with varying O_2 partial pressure at 8 bar total pressure. The upper limit of O_2 partial pressure tested was 1.68 bar, which corresponds to 21 vol% O_2 (air). Decreasing the oxygen partial pressure had minimal effect up to 0.6 bar. Below 0.6 bar, the O_2 partial pressure appeared to hinder the reaction rate at higher conversions, and a slow, solid-state diffusion controlled portion was observed. The onset of the diffusion controlled portion appeared at lower conversions as the partial pressure was decreased. At partial pressures of 0.4 and 0.2 bar O_2, the diffusion controlled portion begins at approximately 40% and 15% conversion. With 0.2 bar O_2, the oxygen carrier takes approximately 5 minutes to reach full conversion.

A number of observations were made in regards to the morphology of the ilmenite particles oxidized in different O_2 partial pressures based on SEM images of the particle's surface shown in Figure 3-12 and the particle's cross section in Figure 3-6.

1) Cracks had formed throughout particle oxidized in 1.68 bar O_2 partial pressure. Figure 3-12 shows the cracks over the entire surface of the particle, and Figure 3-6 shows the cracks through the center of the particle. The particle oxidized at a low O_2 partial pressure (0.2 bar) had not cracked. The stresses inside the particle from rapid volume expansion during the oxidation reaction, during the initial redox cycles cause the formation of cracks [44]. Mattisson et al. attributed the enhanced reactivity over cycles to the increase in surface area for reaction from crack formation [45]. As the

partial pressure decreased below 0.6 bar, it is likely the crack formation on the particle was considerably less, resulting in a significantly slower rate of oxidation.

2) The surface of the particle oxidized at 1.68 bar O_2 had a more tightly packed granular structure whereas the particle oxidized at 0.2 bar O_2 shows a more loose packed morphology. The cross-section of the particle oxidized in 0.2 bar O_2 also appeared considerably less dense.

The distribution of the iron and titanium phases also differ in the particles oxidized at different O_2 partial pressures. EDS mapping of the cross section (Figure 3-6) of the particle oxidized at 0.2 bar O_2 showed a core shell type structure, with an iron shell and a titanium rich core. The migration of iron to the reaction interface is caused by the Kirkendall effect, the same phenomena which causes scale formation on steel[46]. The Fe ions diffuse through the titanium phase to the surface of the particle, causing vacancies and leading to a more porous , titanium rich structure[47]. The core shell type structure was not observed in the particle oxidized at 1.68 bar. Although there was enrichment of Fe and Ti phase across the particle, the intensity was considerably less and the enriched areas were randomly located along the cross-section of the particle.

To confirm the absence of cracks were the cause of the significantly slower kinetics at the lower O_2 partial pressure, a separate test was conducted where the ilmenite particles were activated by conducting 10 oxidation cycles in 1.68 bar O_2, and oxidizing in 0.2 bar O_2 on the 11^{th} cycle. As suspected, the kinetics are significantly faster after having activated the sample in 1.68 bar O_2 when comparing with the sample activated in 0.2 bar O_2, as seen in Figure 3-7.

As previously mentioned, the enhanced kinetics are due to the increase surface area for gas-solid contact with the formation of cracks by activating in 1.68 bar O_2.

Redox cycles in both high and low O_2 concentrations compromise the structural integrity and increase the friability of the particle, through different phenomena however. The increased cracks observed at high O_2 partial pressure would likely cause fragmentation in a circulating fluidized bed. At low O_2 partial pressure, attrition of the iron rich shell would likely occur since the boundary between the core and shell is mechanically weak, as highlighted by the voids in Figure 3-6. Currently, the major use of ilmenite is for the production of titanium dioxide. Attrition of an iron rich shell would refine ilmenite for its titanium content, yielding a value-added product which may be sold in the market. To maximize oxygen carrier use and obtain a titanium rich product, a recycle air stream can be added to the air reactor to maintain a low O_2 partial pressure. The iron rich fines recovered from the cyclone can also be reused as oxygen carrier in the system.

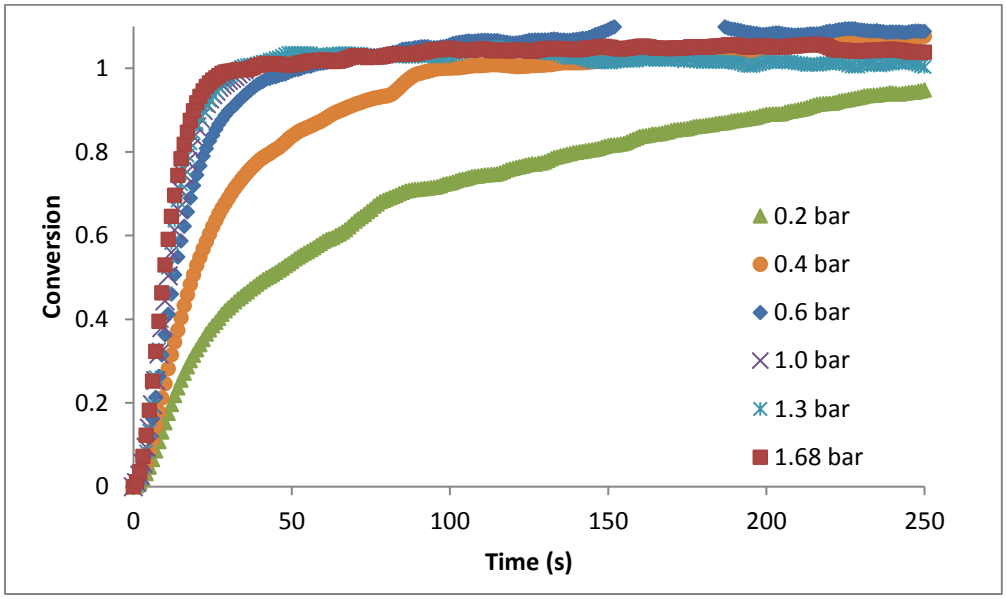

Figure 3-5: Effect of O_2 partial pressure on ilmenite's oxidation. Test conditions: Total ***P***=8 bar, ***T***=900 °C.

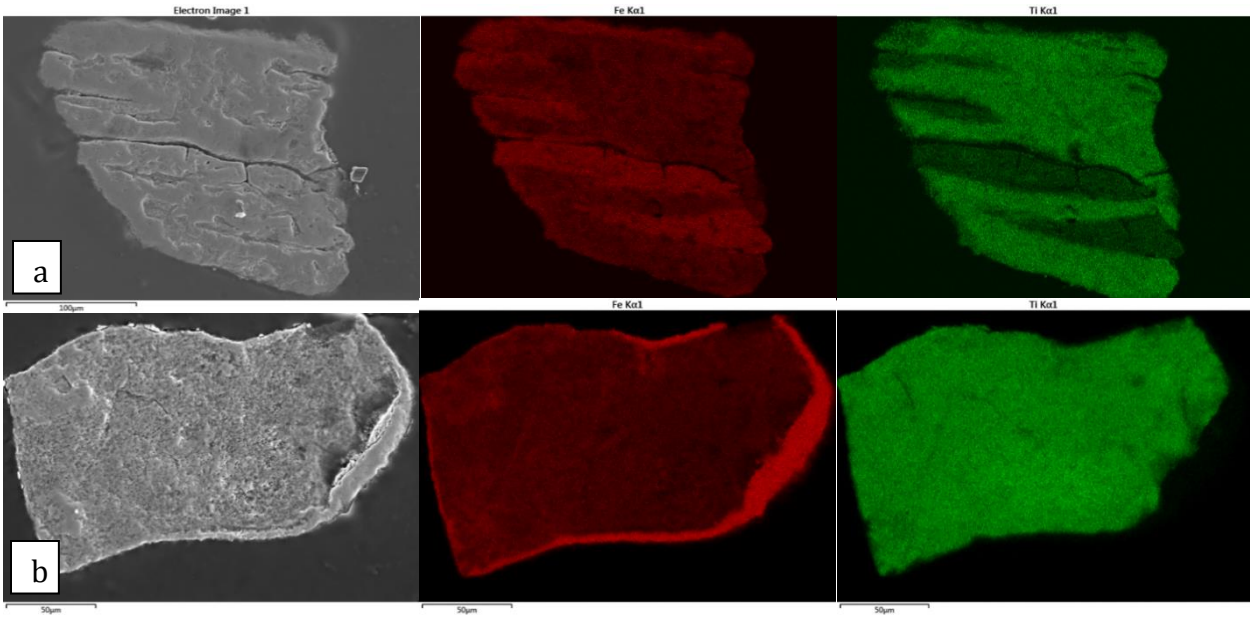

Figure 3-6: SEM EDS mapping of oxidized particle cross section at 8 bar and 900 °C, oxidized with a) 1.68 bar O_2 b) 0.2 bar O_2

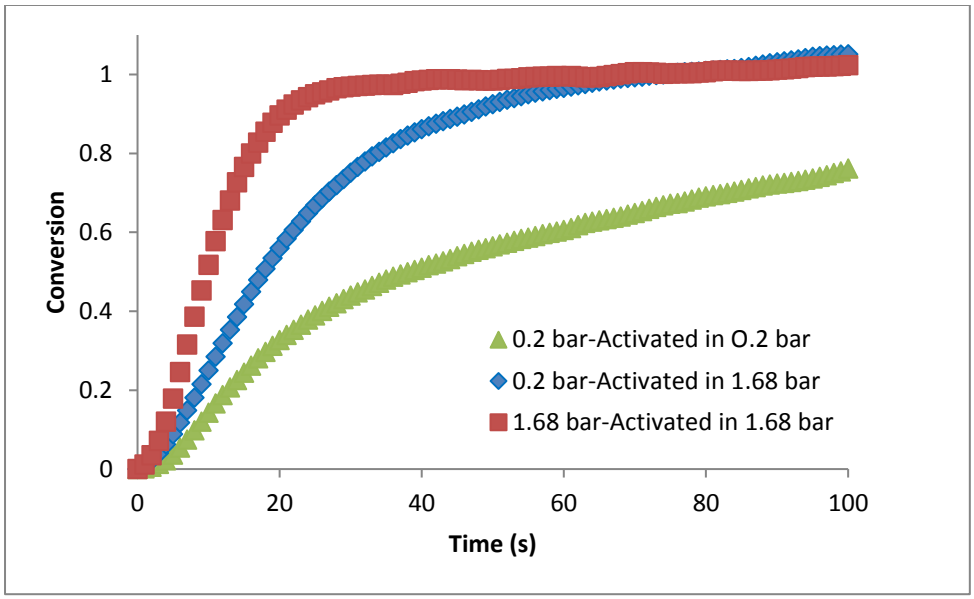

Figure 3-7: Kinetics of oxidation with 0.2 bar O_2 using a sample activated under an oxidizing gas of 1.68 bar O_2 and 0.2 bar O_2. Test conditions: Total ***P***=8 bar, ***T***=900 ^oC.

3.3 Effect of Temperature

The temperature was varied from 800 ^oC to 1000 ^oC. Figure 3-8 shows the resulting conversion curves. At 800 ^oC, a lower carrying capacity is observed. SEM-EDX of the particles shows a more dispersed Ti phase in the 900 ^oC particle, compared with the 800 ^oC sample as shown in Figure 3-9. The Ti phase appears to have separated and agglomerated in the 800 ^oC particles, as there is a more notable contrast between the Ti rich and Ti lean areas. The separation of the Ti and Fe phase suggests the presence of more hematite instead of pseudobrookite, providing evidence to the incomplete oxidation of the ilmenite. As hematite is an intermediary product to the oxidation of ilmenite, it was suspected the oxidation reaction did not reach completion and hematite was formed. With the formation of hematite as the oxidation product, a loss in carrying capacity is expected, as less Fe^{3+} ions are reduced

to Fe^{2+}, and the carrying capacity of the individual ilmenite and hematite species are 5% and 3.3% respectively.

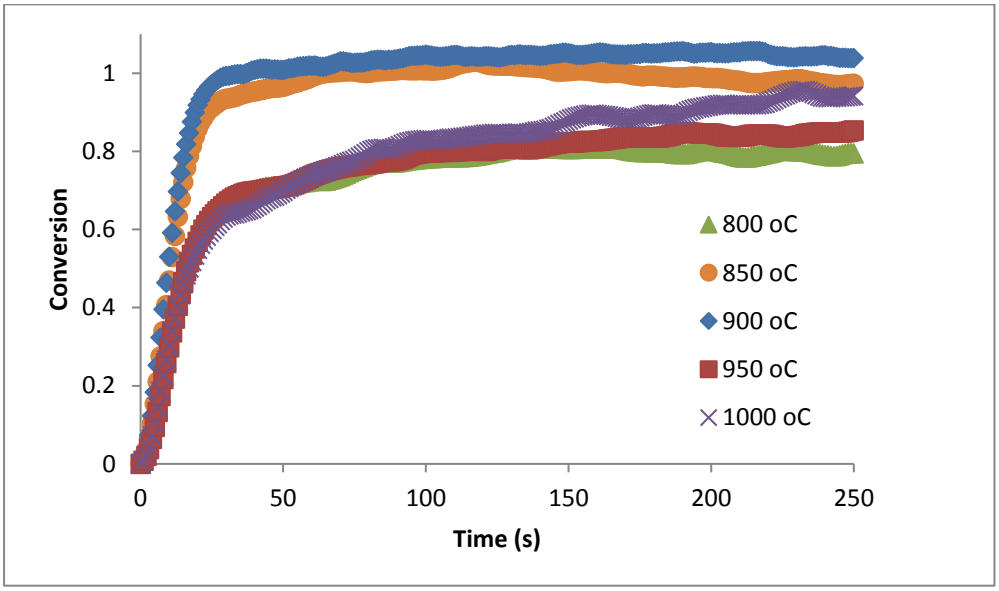

Figure 3-8: Effect of Temperature on ilmenite's oxidation Test conditions: Total $\boldsymbol{P}$=8 bar, $\boldsymbol{Pp_{O_2}}$=1.68 bar.

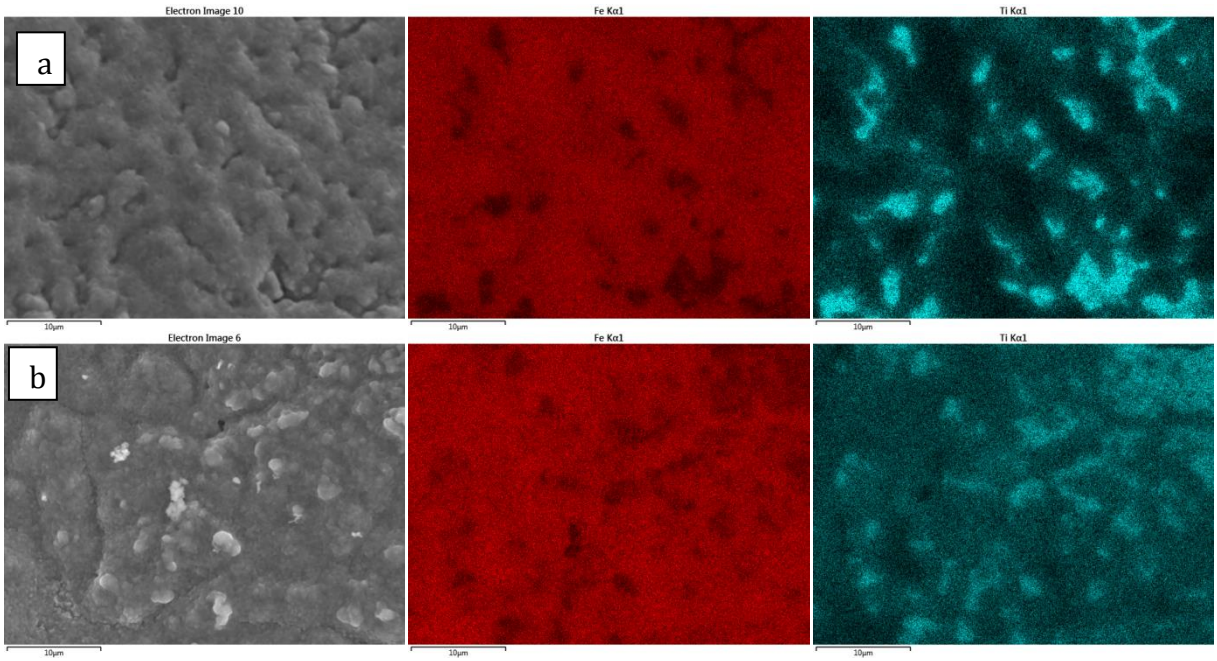

Figure 3-9: SEM EDX mapping of oxidized particle surface. Sample oxidized in air at 8 bar: a) 800 °C b) 900 °C showing the phase densities of iron (red) and titanium (blue)

Mossbauer spectroscopy of the reduced samples of the 800 ^{o}C and 900 ^{o}C was conducted, and the spectra are shown in Figure 3-10. Each spectrum consists of:

- A six-line Zeeman component (cyan solid line), originating from the alpha-Fe_2O_3 phase.
- Two broad Zeeman components (black solid lines), originating from a solid solution of magnetite with a compound of unknown chemical composition
- A quadrupole doublet component (pink solid line), resulting from the ferrous phase of ilmenite
- A broad quadrupole doublet component (brown solid line), originating from a ferrous phase of unknown chemical composition

The results of the Mossbauer Spectroscopy are summarized in Table 3-1. The results confirmed more iron was present as ilmenite at 900 ^{o}C; 33.2% of iron was present as ilmenite at 800 ^{o}C compared with 42.6% at 900 ^{o}C. Iron present as alpha-Fe_2O_3 and iron in the solid solution of magnetite was also found to be more at 800 ^{o}C. The results at 900 ^{o}C showed a broader spectrum due to significantly disordered phases, which gives evidences to the presence of a significant amount of amorphous phase.

In a PCLC process, the air reactor will likely operate at a temperature above 900 ^{o}C, hence the incomplete oxidation at 800 ^{o}C does not pose a problem. However incomplete oxidation is also expected with shorter residence times. Abad et al. found the hematite content to increase over redox cycles when the reaction times were reduced [17], giving a decrease in overall carrying capacity. This can have important implication in a fluidized bed CLC reactor

where, depending on flow regime, several percent of solids will not fully react due to the relatively broad residence time distribution. However Abad et al. also observed the reactivity to increase with the decrease in carrying capacity, because of which the overall oxygen transference (rate of oxygen transfer) remained unaffected. Such phenomenon was not observed in this study; the decrease in carrying capacity due to lower temperature did not result in a faster conversion rate.

Table 3-1: Fe composition of sample in the reduced state oxidized at **a) 800 °C** and **b) 900 °C**

Composition (%Fe)	Sample a	Sample b
alpha-Fe_2O_3 (**Fe^{3+}**)	4.9	1.6
Solid solution with magnetite (**Fe^{3+}, $Fe^{2.5+}$**)	14.8, 28.2	14, 23.6
Ferrous phase in ilmenite (**Fe^{2+}**)	33.2	42.6
Ferrous phase in unknown compound (**Fe^{2+}**)	18.9	18.2

Temperature has a minimal effect on the reactivity between 850 °C and 900 °C, although there is a slight change in carrying capacity, with 900 °C reaching a slightly higher conversion. At 950 °C and above, the rate conversion curve deviates from the trend, due to sintering of the particle. The clogging of mesopores decreases the direct gas-solid contact area and hinders the access of the oxygen to the reaction sites. However the conversion continues increasing slowly after the fast portion of the reaction, indicating solid-state diffusion of the ions. It is also possible the sintering of the particle preferred conversion to hematite, due to the inaccessibility of the titanium which remains inside the particle upon the Fe atoms segregating to the boundaries. This would explain the similar conversion curves at 800, 950 and 1000 °C.

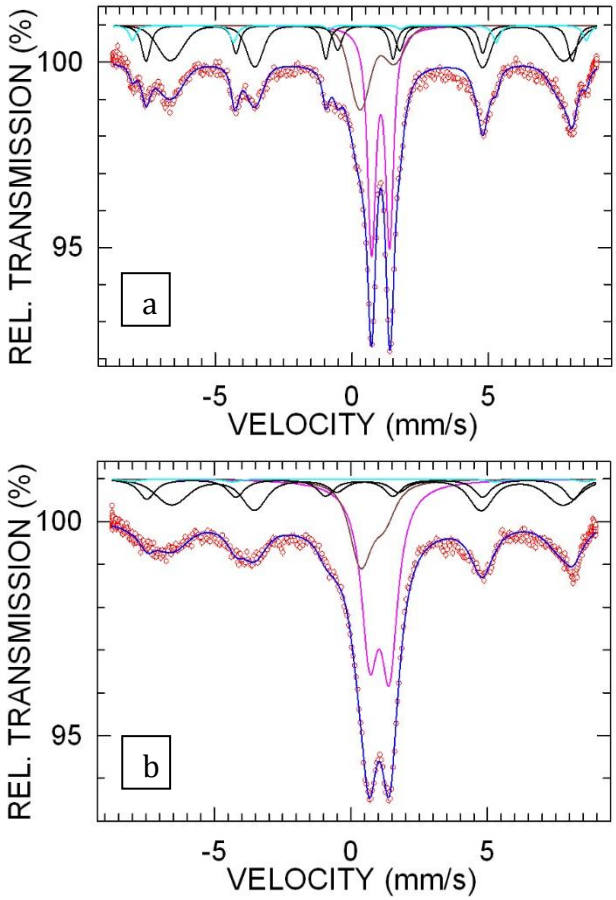

Figure 3-10: Mossbaeur spectrum of sample in the reduced state, oxidizing conditions: P=8 bar, Pp_{O2} =1.68 bar, **a)**T= 800 ^{o}C **b)**T= 900 ^{o}C

The temperature was varied by 25 ^{o}C intervals from 800 to 950 ^{o}C to narrow the range where the transition occurs in rate. As seen in Figure 3-11, the kinetics begins to deviate from the trend, in that a lower rate is observed at a higher temperature, at 925 ^{o}C. Although the sintering temperature of the species present in the ore under the specified operating conditions are predicted to have melting temperatures well above the tested range. It is possible that trace amount of elemental iron is present in the ore at the reaction front. A number of authors observed the presence of metallic iron, which had precipitated to the

periphery of the particle, after reducing with CO, however under temperature higher than 1200 °C or reduction times longer than 30 mins [48]. A phase transition also occurs in the crystalline structure of metallic iron at 912 °C [49]. The crystallographic configuration of iron changes from Body-Centered Cubic (BCC) to Face-Centered Cubic (FCC). This transition in phases is possibly the cause of the sintering and resulting reduced performance observed above 900 °C. However metallic iron must be identified prior to arriving at a definitive conclusion, as the reduction to metallic iron is not expected with CO_2 in the reducing gas mixture.

Due to the variation in oxidation products with temperature, and sintering effects, a narrow temperature range is used for the oxidation kinetic model. The activation energy is derived for a temperature range of 850-900 °C.

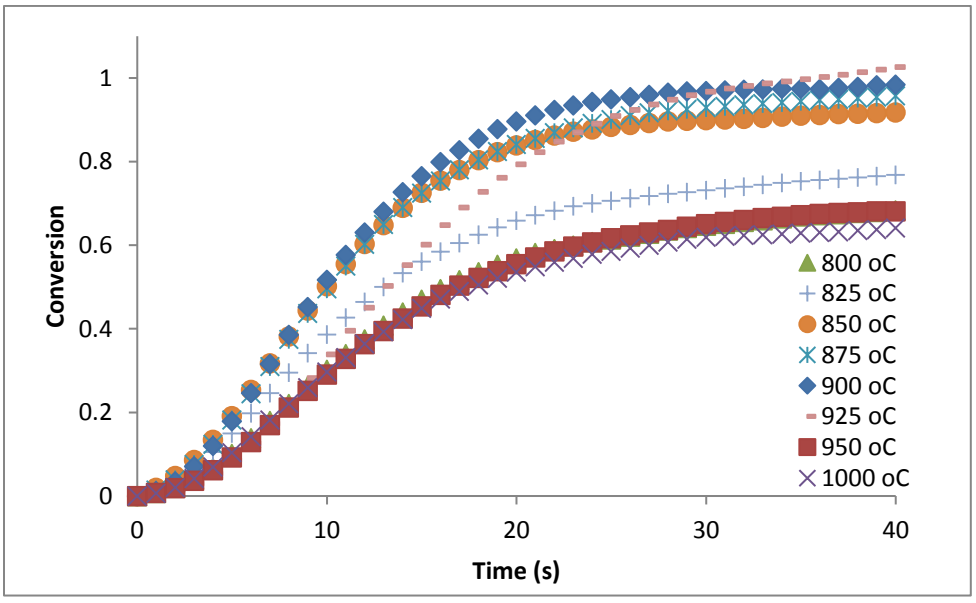

Figure 3-11: Reduced temperature intervals to observe the effect of Temperature on ilmenite's oxidation. Test conditions: Total $\boldsymbol{P}$=8 bar, $\boldsymbol{Pp_{O_2}}$=1.68 bar.

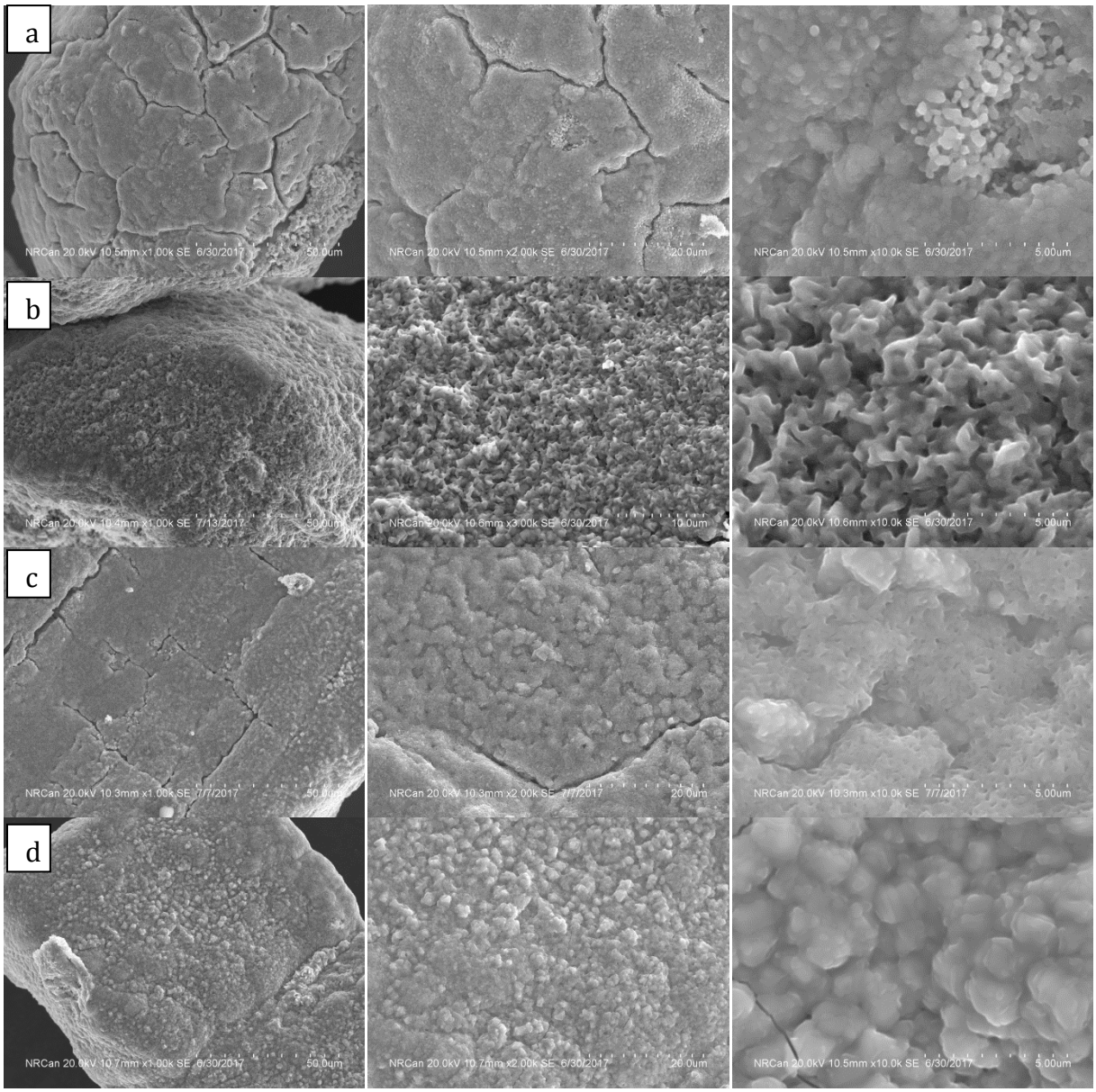

Figure 3-12: SEM images of ilmenite particles after 10th cycle oxidation at 8 bar in a) Air at 900 °C b) 0.2 bar O_2 at 900 °C c) Air at 800 °C and d) Air at 1000 °C

3.4 Effect of Total Pressure

3.4.1 Constant Gas Composition

The effect of the operating pressure on the oxidation kinetics is of interest, as the operating pressure in PCLC is determined independently of kinetics. Higher operating pressures are expected to have a positive effect on reaction kinetics. The O_2 partial pressure increases in proportion with pressure since oxidizing gas composition entering the air reactor remains unchanged at 21vol% O_2, corresponding to the oxygen content in air. Hence both the oxygen partial pressure and the total system pressure is changing. Figure 3-13 shows the enhanced kinetics with an increase in pressure, up until 8 bar, above which increasing the pressure had a minimal impact on kinetic data. From 8 bar to 12 bar, the change in rate is minor. Between 12 and 16 bar, no change is observed in the kinetics, and the oxidation kinetics are unaffected by pressure. This coincides with the varying O_2 partial pressure tests conducted at 8 bar, where the effect of O_2 partial pressure was insignificant above a threshold. It is difficult to derive any conclusions based on SEM images in Figure 3-15, as the differences in morphology are not obvious.

It must be noted that at 1 bar, the same level of conversion is not reached as the high pressure tests, likely due to the lower methane partial pressures in the reduction cycle. As seen in Figure 3-14, with an increase in methane fraction from 15 vol% to 30 vol%, the particle conversion also increases, however the initial, fast part of the conversion curve is not significantly altered. The methane partial pressure obtained at atmospheric conditions

is incomparable to that of higher pressure tests. The methane fraction was not increased beyond 30 vol%, to maintain the 2:1 ratio of CO_2:CH_4 used in all experiments.

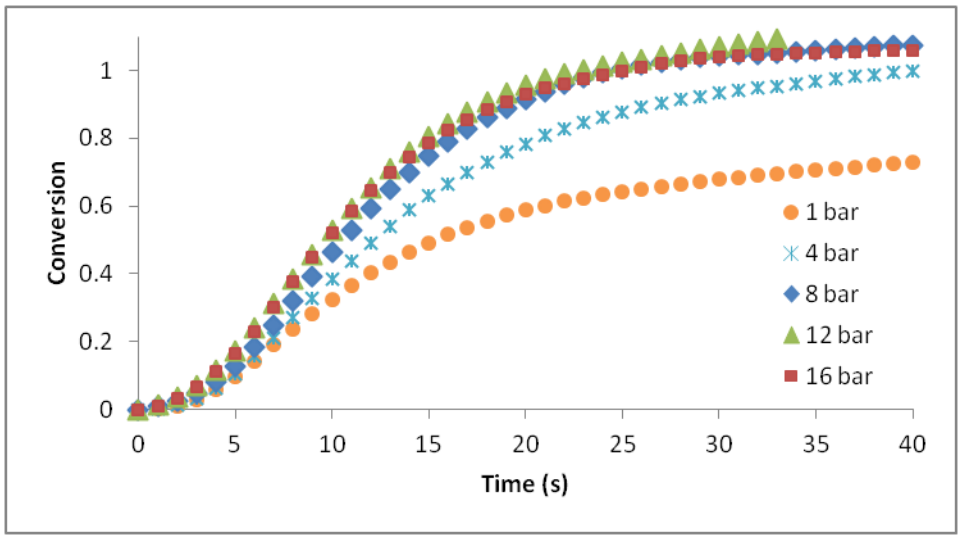

Figure 3-13: Effect of Pressure on oxidation kinetics with 21 vol% O2. Test conditions: $\boldsymbol{T}$=900 °C.

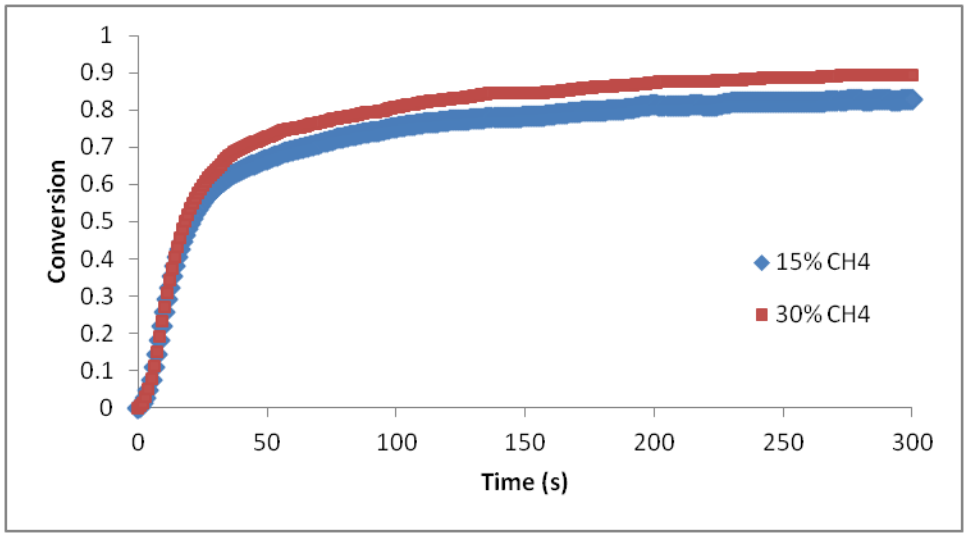

Figure 3-14: Effect of reducing gas composition on oxidation. Test conditions: $\boldsymbol{P}$=1 bar, $\boldsymbol{T}$= 900 °C, $\boldsymbol{Pp_{O_2}}$=0.21 bar O2.

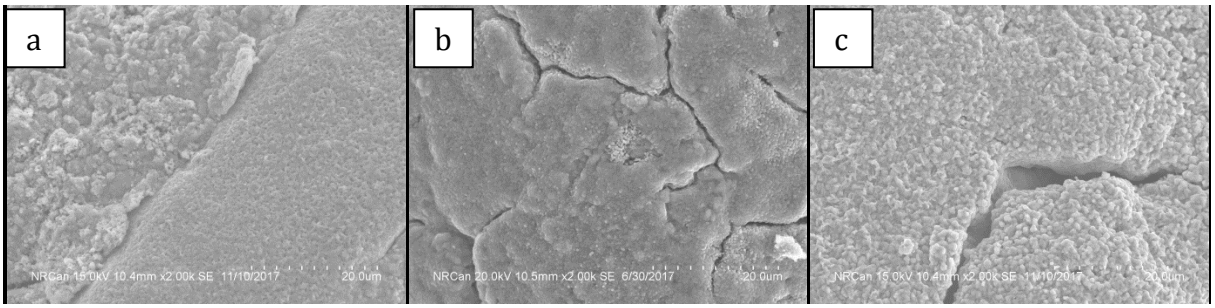

Figure 3-15: SEM images of particle oxidized with 0.21 vol% O_2 at a total pressure of a) 1 bar b) 8 bar c) 16 bar

3.4.2 Constant O_2 Partial Pressure

To isolate for the effect of system pressure, the total pressure was varied while maintaining a constant O_2 partial pressure. The pressure has a negative impact on the reaction kinetics, as seen in Figure 3-16. The effect is more significant at lower O_2 partial pressures. The observed decrease in reaction rate with pressure at 0.2 bar O_2 was prominent compared with a partial pressure of 1.7 bar O_2.

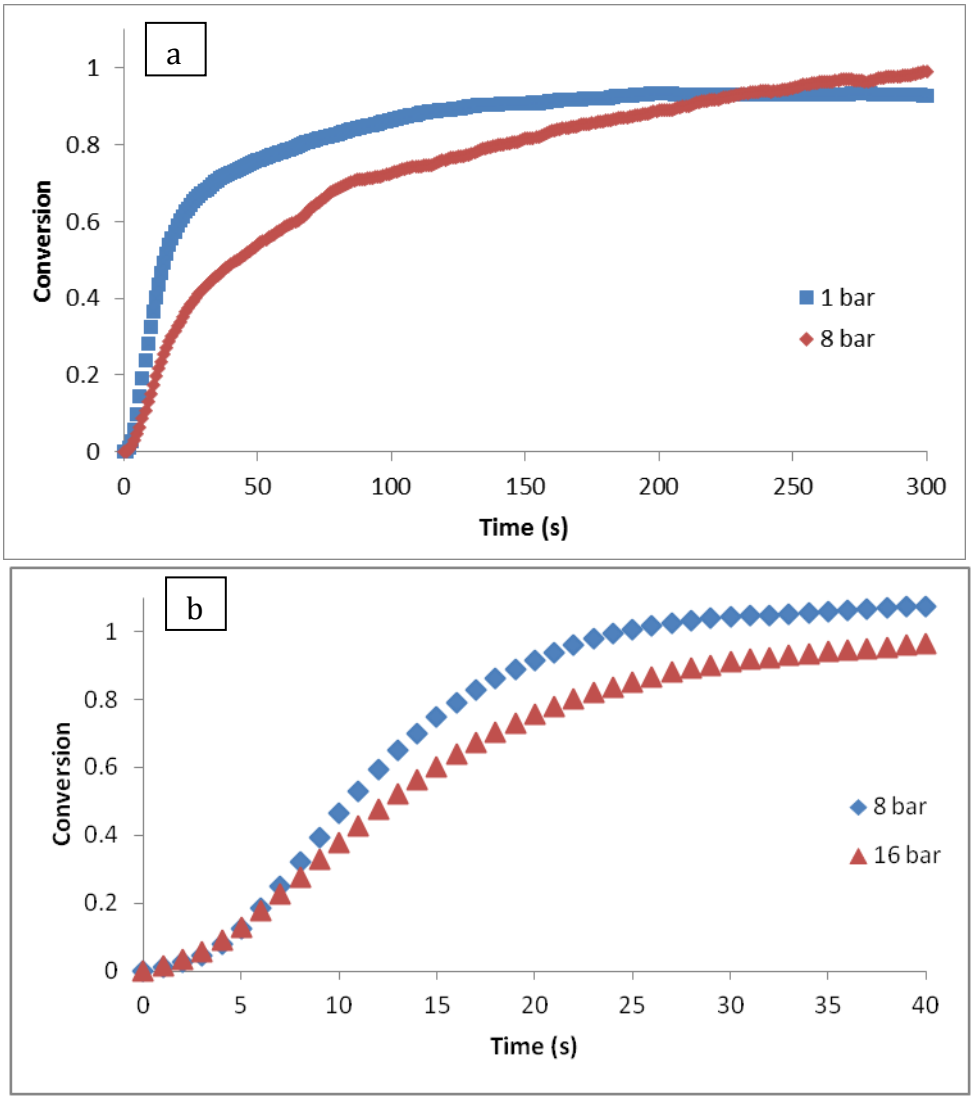

Figure 3-16: Effect of Pressure on oxidation kinetics with constant O_2 partial pressure. Test conditions: $\boldsymbol{T}$ =900 °C, a) $\boldsymbol{Pp_{O_2}}$=0.2 bar b) $\boldsymbol{Pp_{O_2}}$=1.7 bar.

3.5 Oxidation Behaviour of a Partially Reduced Sample

The PTGA experiments were conducted with a sufficient reduction time to ensure the sample reduced to the lowest possible oxidation state. However, in a reactor system, there is a possibility the particles will not fully reduce in the fuel reactor, and enter the air reactor in a partially oxidized state, either due to reactor design or a broad residence time distribution

in the reactor. To analyze the oxidation kinetic behaviour of a partially oxidized sample, the reduction cycle was decreased to 40 s, which halted the reduction approximately halfway. Figure 3-17 shows the oxidation kinetics of a partially reduced sample, compared with the base case of complete reduction. From the experimental data, the mass change during the partially reduced test was observed to be 2.2%, hence the data was normalized to an R_{oc} of 2.2%. Commencing the reaction from a higher oxidation state did not change the oxidation kinetic behaviour, as seen in Figure 3-17. This does not coincide with the observation of Abad et. al of an increase reactivity with a decrease in oxygen carrying capacity at atmospheric pressure, as mentioned in Section 3.3 "Effect of Temperature".

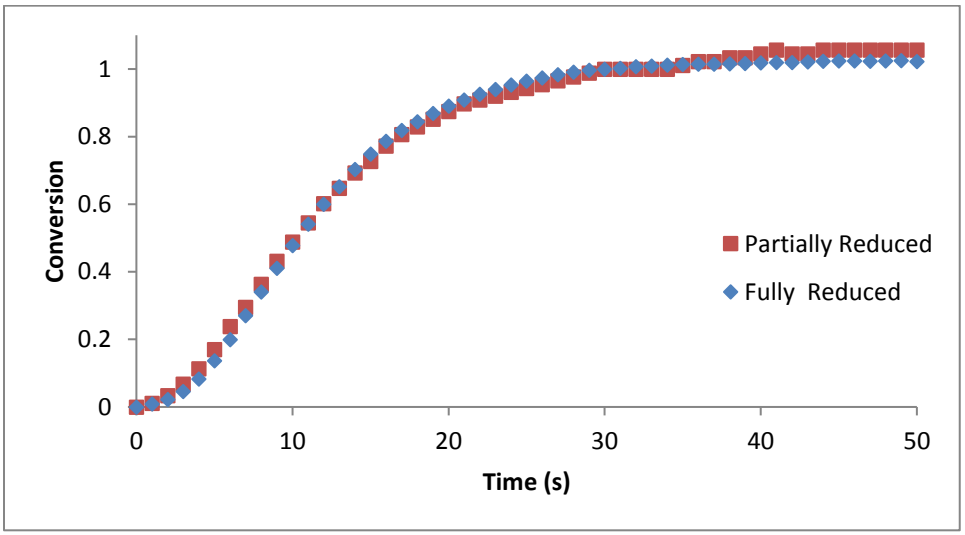

Figure 3-17: Oxidation behaviour of a partially reduced sample. Test conditions: $\boldsymbol{P}$=8 bar, $\boldsymbol{T}$=900 °C, $\boldsymbol{Pp_{O2}}$ = 1.68 bar

3.6 Kinetic Model

Although the changing grain size or the shrinking core model is typically used to model redox kinetics in CLC, most authors have acknowledged the data fitting nature of the model [50]. To gain insight into the reaction mechanism, Avrami-Erofeev plots were generated for each test condition. The Avrami -Erofeev plots showed a linear trend for the initial part of the reaction, then begins to diverge from the linear trend. This indicates the presence of a secondary mechanistic regime which begins to dominate as the reaction progresses. The dominance of the secondary regime occurs earlier for the low oxygen partial pressure tests than for the high oxygen partial pressure tests, as seen in Figure 3-18. For conditions which demonstrated the presence of two distinct regimes, a fast initial portion and a slower latter portion, such as with 0.2 bar O_2, the Avrami-Erofeev plot showed two distinct portions, as seen in Figure 3-18b. The slope of the plot fast portion varied from 1.7-2.1, indicating 2-D nucleation and growth as the rate controlling process during the initial portion of the reaction. The slow latter portion observed at lower O_2 partial pressures best fit Jander's diffusion equation (D_3). Hence these two rate expressions were used to model the oxidation kinetics.

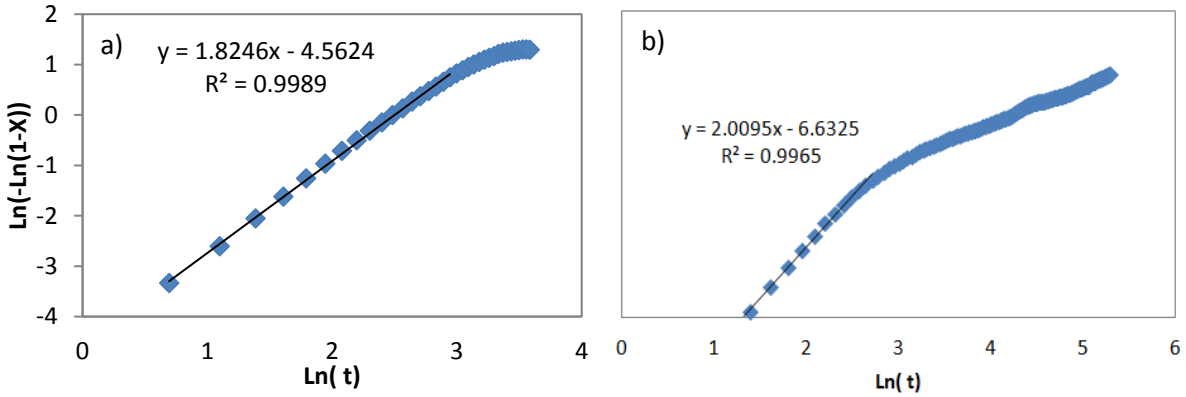

Figure 3-18: Avrami-Erofeev plot for Oxidation Reaction at 8 bar and 900 °C in a) Air b) 0.2 bar O_2

The 2nd order nucleation model and the Jander diffusion model are shown below. The Jander diffusion model is applied after the transition point, whereas the nucleation and growth model is applied before. The transition point occurs at different conversions for different test conditions. Table 3-2 details the transition point for each test, which was determined by minimizing the R^2 of the model fit onto experimental data. This transition point increases with increasing O_2 partial pressures, until about 1.0 bar O_2. Above 1.0 bar O_2, the transition point remains constant around 0.80.

$$\frac{t_{nuc}}{\tau_{i,nuc}} = [-\ln(1-X)]^{\frac{1}{2}} \tag{12}$$

$$\frac{t_{diff}}{\tau_{i,diff}} = \left[1-(1-X)^{\frac{1}{3}}\right]^2 \tag{13}$$

$$t = t_{diff} + t_{nuc}|_{X_{tr}} \tag{14}$$

Table 3-2 also details the experiments used and the respective test parameters used in deriving the oxidation kinetic model. Tests 1-6 were used with Equation 15 to determine the order of reaction graphically with respect of oxygen. Test 6-8 were used along with Equation 16 to generate an Arrhenius plot, and determine the activation energy. The plots to determine the order of reaction and the Arrhenius plot are shown in Figure 3-19 and Figure 3-20 respectively.

Table 3-2: Summary of Experiments used in the derivation of an oxidation kinetic model at 8 bar

Test #	O_2 partial pressure (bar)	Temperature (°C)	τ_{nuc} (s)	τ_{diff} (s)	X_{tr}
1	0.2	900	25.0	714	0.15
2	0.4	900	18.9	250	0.4
3	0.6	900	14.9	96.2	0.65
4	1.0	900	13.2	66.7	0.8
5	1.3	900	13.0	60.6	0.75
6	1.68	900	12.2	50.0	0.85
7	1.68	875	12.8	58.8	0.70*
8	1.68	850	13.2	62.5	0.70*

* The overall oxygen transport capacity is lower for the low temperature runs. At 800 °C, an overall carrying capacity of 4.0% is achieved. The value of Xtr given was normalizing with an R_o of 4.3% for all runs.

$$\ln(\tau_i) = \ln\left(\frac{\tau_i'}{e^{\left(-\frac{E_a}{RT}\right)}}\right) - n\ln(C_g) \quad (15)$$

$$\ln(\tau_i) = \ln\left(\frac{\tau_i'}{C_g^n}\right) + \frac{E_a}{R}\cdot\frac{1}{T} \quad (16)$$

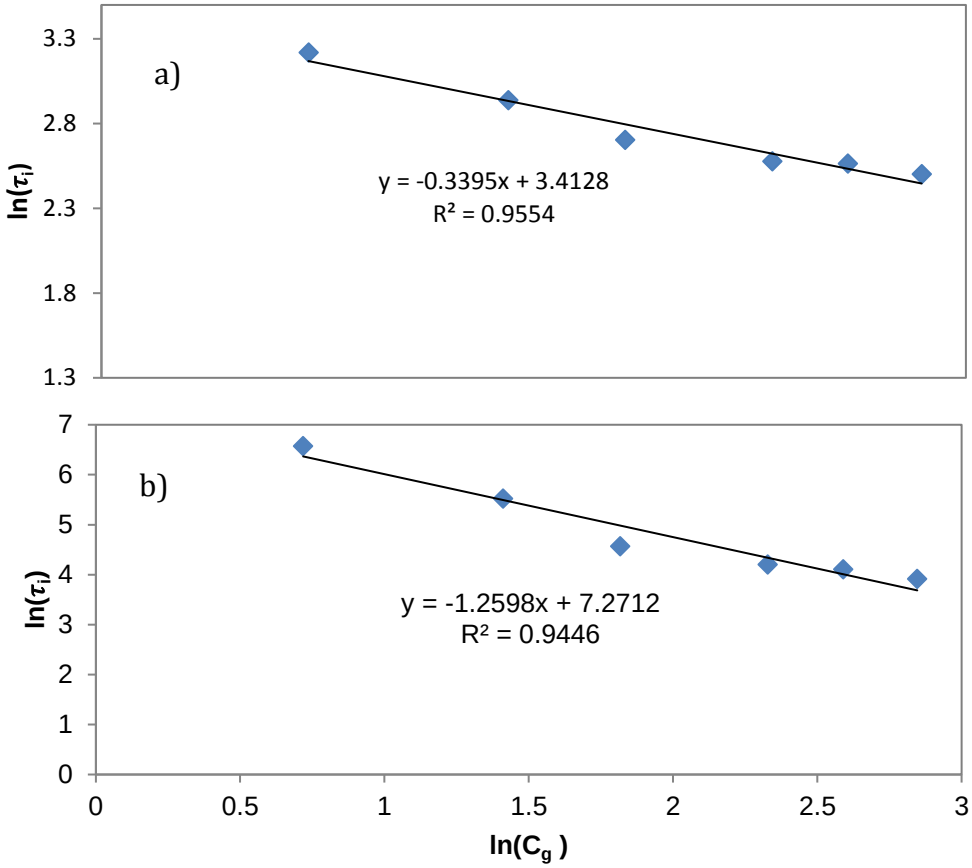

Figure 3-19: Plot to obtain reaction order with respect to oxygen for a) Nucleation and Growth Controlled Regime b) Solid State Diffusion Controlled Regime

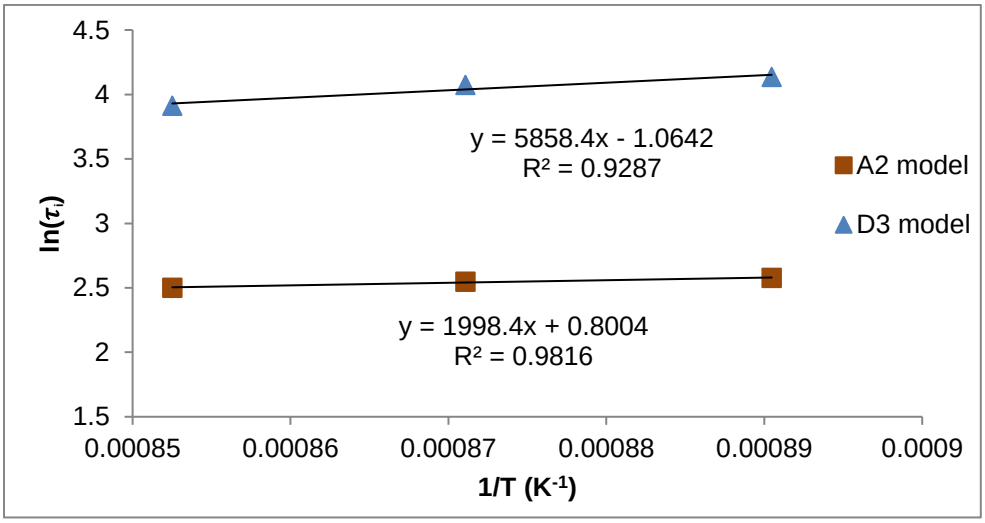

Figure 3-20: Arrhenius Plot for the determination of the activation energy for the nucleation model

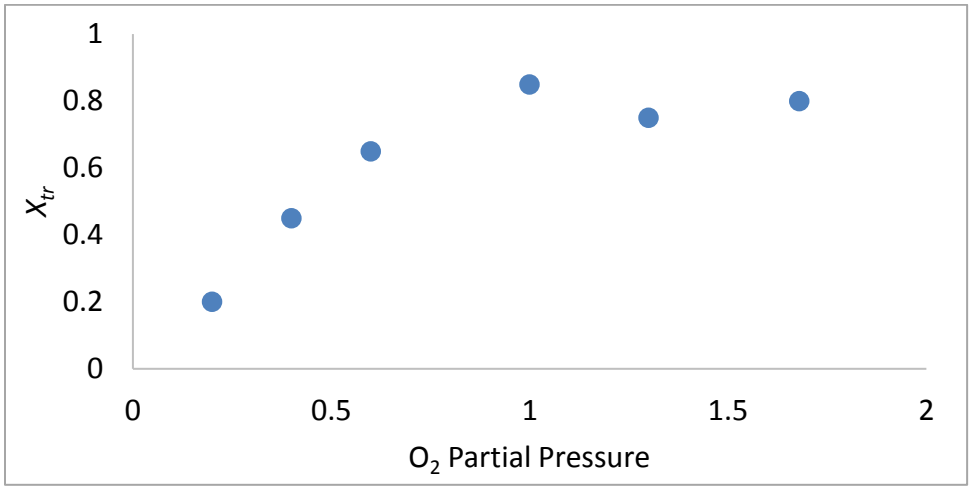

Figure 3-21: The transition point from the nucleation and growth model to the solid state diffusion model at 8 bar

Table 3-3: Summary of Kinetic Parameters for oxidation reaction at 8 bar

Kinetic Parameters	2-D Nucleation and Growth Model	Jander's Diffusion Model
n	0.3	1.3
E_a (kJ/mol)	16.6	48.7
τ_i'	5.9	12.8

The model provided a reasonable fit to the data, as seen in Figure 3-22. The transition of the models is blunt, and further development of the kinetic models would illicit the two rate expression being applied in parallel, as the two mechanism likely overlap. The intermediary partial pressure tests (0.4 and 0.6 bar O_2) provide the worst fit, likely due to the overlap of the mechanisms being significant for these tests.

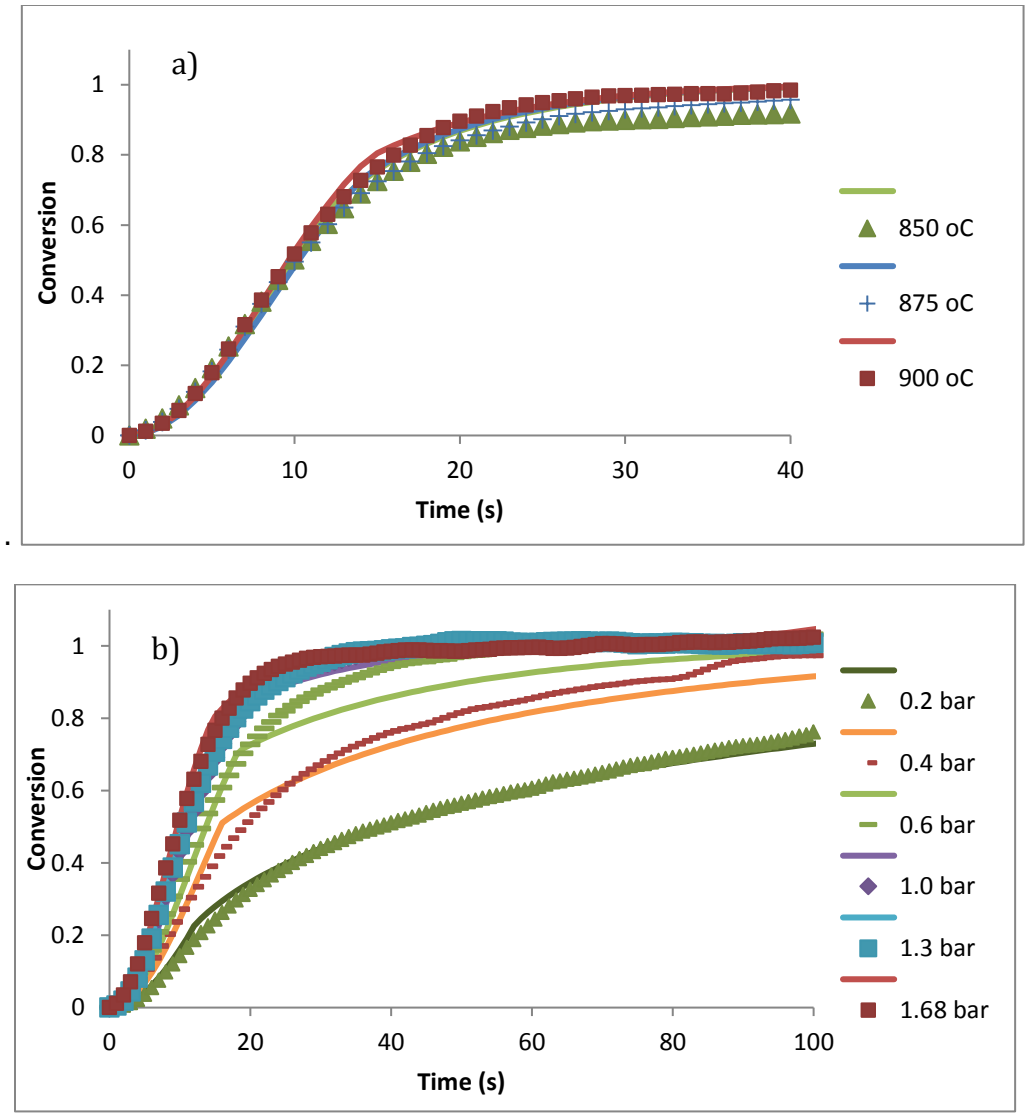

Figure 3-22: Oxidation Kinetic Model fit with Experimental Data a) varying temperature b) varying partial pressure. Line=Model Predictions, Dots=Experimental Results

The oxidation of metals is typically limited by solid-state ionic diffusion through the product layer and the reaction obeys the parabolic rate law[51][52]. The Jander equation is the modified expression of the parabolic rate for spherical particles. Due to the higher surface area to volume ratio of ilmenite microparticles, added with the crack formation caused by

the stresses from volume expansion of the oxygen diffusion during the initial redox cycles, and the pore formation inside the particle from the outward diffusion of Fe and Ti ions [44], the available gas-solid contact area is relatively high. For this reason, the Jander diffusion equation is not applicable for the initial part of the oxidation reaction. However for the latter portion, once an oxide product layer is formed, the Jander diffusion model dominates the reaction. At low partial pressure, the Jander diffusion model dominates for a larger portion of the reaction, since cracks do not form. Without the cracks, intra-particle ion diffusion becomes the controlling mechanism once the oxygen has reacted with the surface Fe ions.

The kinetic model is in accordance with Lv et al. who studied the oxidation reaction of ilmenite for temperatures of 600-1200 ^{o}C and atmospheric pressure. A dual mechanism for the reaction scheme, random nucleation and growth and solid-state diffusion[53]. Similar to the findings in this study, where the dominance of each mechanism varies with test conditions, they found the nucleation and growth to dominate from 1000 ^{o}C to 1200 ^{o}C, and the intraparticle or solid-state diffusion to dominate between 600-700 ^{o}C. The temperatures in between had not modelled, however the application of both mechanisms in that range was proposed. The activation energy for the nucleation and growth controlled range was found to be 4.11 kJ/mol, and the solid-state diffusion controlled range to be 199.43 kJ/mol. Monazam et al. also proposed a two-stage mechanism for the oxidation of magnetite at atmospheric pressure, with the same reaction scheme; nucleation and growth followed by solid-state diffusion [54]. The mechanisms were applied in parallel and a weighing factor was used for each mechanism, which varied with the progression of the reaction. The nucleation and growth process was found to have a low activation energy of 4.21 kJ/mol, and

the solid state diffusion process an activation energy of 53.58 kJ/mol. Abad et. al used the shrinking core model, which is one of the geometric contraction model in Table 2-3, to model the oxidation reaction of ilmenite at atmospheric pressure, and found the activation energy and order of reaction with respect to oxygen to be 25.5 kJ/mol and 1 respectively[43].

In the present study, the activation energy derived for the narrow temperature range of 850-900 ^{o}C was 16.6 kJ/mol for the nucleation and growth mechanism, which is slightly higher than those found in the previously mentioned studies done at atmospheric pressure. The activation energy for solid-state diffusion through the product layer is 48.7 kJ/mol, similar to the value found by Monazam et al. for Magnetite's oxidation.

Chapter 4 -Preliminary Air Reactor Model

4.1 Introduction

Many reactor configurations are possible in a PCLC system. The most common type is the interconnected fluidized beds, in which both the air and fuel reactors operate as circulating fluidized beds, decoupled to allow for better solids control. Another configuration proven successful at the pilot scale is the countercurrent moving bed configuration[55]. The main difference between the two configurations is the larger particle diameter and the gas velocity which is maintained below the minimum fluidization velocity with the moving bed configuration.

Reactor modelling efforts have included one dimensional, single phase models in the axial direction, to multi-phase, core-annular type models. Increasing emphasis is placed on CFD modelling as the hydrodynamics are difficult to predict with the relatively dense metal oxide particles. In this study, a turbulent bed is designed as the air reactor for a 600 kWth pilot scale PCLC unit, to allow sufficient residence time, and maximize gas solid contacting and heat transfer[56].

4.2 Governing Design Equations:

Mass Balance:

The turbulent bed is modelled as axially dispersed in both the gas and solid phases. The overall mass balance in the gas and solid phases are shown below in Equations 17 and 18 respectively:

$$U_g \frac{dC_{i,g}}{dz} - D_{z,g} \frac{d^2C_{i,g}}{dz^2} + r_{i,g} = 0 \tag{17}$$

$$v_p \frac{dC_{i,s}}{dz} - D_{z,s} \frac{d^2C_{i,s}}{dz^2} + r_{i,s} = 0 \tag{18}$$

Hydrodynamics:

Due to the complexity of the reaction scheme, the dispersion coefficients were set to insignificantly low values in the current study. This was done to attain convergence for the preliminary air reactor model. However, the dispersion coefficients are significant in a turbulent bed due to the well-mixed nature. Upon further development of the model in the future, the following correlations are to be used calculate the gas phase and solid phase axial dispersion coefficients[57]:

$$Pe_g = \frac{Ul}{D_{z,g}} = 3.47Ar^{0.149}Re^{0.0234}Sc^{-0.231}\left(\frac{l}{d}\right)^{0.285} \tag{19}$$

$$Pe_s = \frac{v_p l}{D_{z,s}} = 4.22x10^{-3}\,Ar \tag{20}$$

Reaction Scheme:

The rate expression applied to the reactor model is show in Equations 21 and 22. The specific rate of reaction for ilmenite's oxidation was derived in Section 3.6 "Kinetic Model" based on TGA experiments. The specific rate expression is given in Table 2-3 (Models A_2 and D_3) and the kinetic parameters can be found in Table 3-3.

$$r_i = \frac{\rho_{oc} R_{oc}}{M_o}(1-\epsilon)\frac{dX}{dt} \tag{21}$$

$$\frac{dX}{dt} = \begin{cases} \frac{dX}{dt}|_{nuc,}, & X < X_t \\ \frac{dX}{dt}|_{diff}, & X \geq X_t \end{cases} \tag{22}$$

Pressure Drop:

The pressure differential below was used to determine the pressure drop across the fluidized bed, which is mainly due to hydrostatic forces[58].

$$\frac{dP}{dz} = -g[\,\rho_p\,(1-\epsilon) + \rho_g \epsilon] \tag{23}$$

4.3 Design Specifications:

The reactor system is considered for a pilot scale unit with a thermal input of 600 kW LHV. As mentioned in Chapter 1, minimizing excess air exiting the air reactor is critical for PCLC to be economically feasible. Hence, an air to fuel ratio of 1.05 was used. The solid circulation rate was set with a 10% excess. Note that an insufficient circulation rate would lead to

unconverted fuel. Higher solid circulation rate means solids are converted to a lower extent and the operating costs are higher, however the capital cost may be less as the rate of reaction is slower at higher conversions, as can be seen from Figure 3-1. Upon further development of the air reactor model and the hydrodynamics, case studies must be performed on the solid circulation rate and the air to fuel ratio to determine the optimal operating conditions.

The diameter of the turbulent bed was specified to achieve the desired fluidization regime. The onset of the fast fluidization regime was calculated by Equation 25, which corresponded to a diameter of 0.20 m. The onset of the turbulent regime was calculated by Equation 24 [59], which corresponded to a diameter of 0.37 m. The turbulent regime, with the given flowrate, is found within this range of diameters. A diameter of 0.22 m was chosen as the entrainment of solids also increases with an increase in velocity, and is an important parameter due to the circulation of solids. The reactor length or bed height was chosen to be approximately 3 times the diameter, however in the future, case studies must be performed to optimize this parameter, as dispersion in the bed and oxygen conversion is strongly affected by the bed height.

$$Re_c = 0.565Ar^{0.461} \tag{24}$$

$$Re_{se} = 1.53Ar^{0.5} \tag{25}$$

The solid-holdups in a turbulent bed are 0.25-0.35, hence an average was used and 0.3 was set as the solid hold-up. Based on this value, and the solid flux, the particle velocity was calculated by Equation 26.

$$v_p = \frac{G_s}{\rho_p \epsilon_s} \tag{26}$$

The temperature and pressure were determined through process studies to optimize power recovery. The operating conditions and design specifications for the air reactor are given in Table 4-1. Ilmenite's physical properties applied to the reaction scheme and fluidization calculations are given in Table 4-2.

Table 4-1: Air Reactor Model Operating Conditions and Design Specifications

	Value
Operating Conditions	
Temperature (^oC)	1020
Pressure (bar)	8
Air to Fuel ratio	1.05
Gas Flowrate (kg/s)	0.19
Solids Circulation Rate (kg/s)	1.15
Hydrodynamic Parameters	
Solid Hold-up (-)	0.3
Reactor Size	
Diameter (m)	0.22
Length (m)	0.70

Table 4-2: Physical Properties of Ilmenite

Physical Property	Value
Density (kg/m^3)	4400
Oxygen Carrying Capacity (wt%)	4.3
Mean Particle Diameter (μm)	147

4.4 Method of Solving:

Dankwert's boundary conditions are applied to the problem second order ODE's, which are as follow:

$$@z = 0; \quad uC_i - D_{ax}\frac{dC_i}{dz}|_{z=0} = u_s C_{i,feed} \tag{27}$$

$$@z = L; \quad \frac{dC_i}{dz}|_{z=L} = 0 \tag{28}$$

The first boundary condition is applied at the tube entrance and is derived based on the feed being diluted as soon as it enters the reactor due to axial mixing (similar to a CSTR). This boundary condition is a mass balance at the reactor entrance, equating the amount of feed before the reactor entrance, where there is no mixing, to the feed downstream the reactor entrance from convective forces and mixing. The secondary boundary condition, applied at the reactor exit, states that the concentration stops changing as the effluent exits the reactor[60].

The second order ODE's were rewritten as sets of first order ODE's. The coupled first order ODE's were solved in MATLAB using the built-in function, `bvp4c`. This function requires the user to specify initial guesses for the independent variables as well as a mesh size. The boundary value problems are solved using a cubic polynomial to approximate the true solution within the intervals of the grid.

4.5 Air Reactor Performance:

The conversion vs. reactor length plot in Figure 4-1 shows 80% gas conversion is achieved at 0.7 m. Due to the dual-mechanistic and transitionary nature of the reaction model, the conversion curves attained are not smooth. The reaction rate integrated into the reactor model was derived in Section 3.6 “Kinetic Model”, and consist of nucleation and growth dominating at low conversions, followed by solid-state diffusion dominating at higher conversion. The transition between the two mechanisms in the kinetic model was blunt, however an overlapping model would be better representative of the system. Further development of the reactor model and the hydrodynamic parameters are also required to arrive at reliable results. The solid hold-ups and dispersion coefficients must be further studies and validated for a reliable performance assessment.

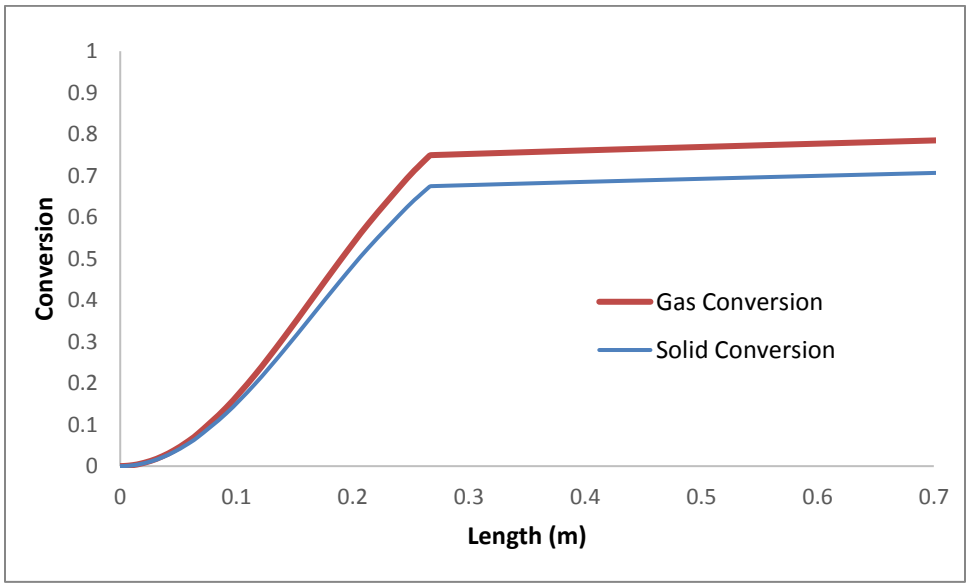

Figure 4-1: Air Reactor Performance for a simplified Turbulent Bed Model

Chapter 5 -Conclusion and Recommendations

Ilmenite's oxidation kinetics for PCLC at 8 bar were modelled using a two-step mechanism to represent the fast and slow portions observed. 2nd order random nucleation and growth followed by Jander's solid-state diffusion was found to be applicable to the oxidation reaction at various conversions. The transition from the nucleation and growth to the solid-state diffusion-controlled mechanism was found to be at higher conversions for higher oxygen partial pressures.

The temperature ranges had a significant effect on the phases formed in the ilmenite ore. At temperatures of 800 ^{o}C and below, the oxidation reaction did not reach completion, resulting in the formation of intermediary products: Fe_2O_3 and TiO_2. At temperatures above 900 ^{o}C, sintering was observed. A temperature range of 850-900 ^{o}C was used to model the kinetics, over which temperature had a minimal effect on the reaction rate. At higher oxygen partial pressures, fissures were observed throughout the particles. The O_2 partial pressure did not have a significant effect on the reactivity, except below 0.6 bar, where the transition to the solid-state diffusion model occurred at lower conversions. This was due to the absence of cracks, and the resulting lower surface area for reaction.

The order of reaction for the nucleation and growth model was found to be 0.3, and the activation energy 16.6 kJ/mol for the narrow range tested. The order of reaction for the Jander diffusion model was found to be 1.3 and the activation energy was found to be 48.7 kJ/mol.

The following are recommendations for future work:

- The performance of ilmenite was found to be poor at temperatures above 900 ^{o}C, due to sintering of the particles. As the air reactor will likely operate at temperatures above 900 ^{o}C, for ilmenite to be a serious contender as an oxygen carrier in PCLC, the cause of the sintering must be addressed.
- The structural integrity of the particle must be further studied, as SEM imaging of the particles identified significant cracking or void formation, which would result in low mechanical stability. Attrition and elutriation would be a major problem in a fluidized bed PCLC system with the natural ore. A moving bed configuration for the reactor system is an option which could reduce oxygen carrier loss through attrition.
- Experiments with reduced oxidation time are also recommended to assess the kinetic behaviour and confirm the predicted phase changes of ilmenite expected with lower reaction times. Due to the fast oxidation reaction, and the difficulty in flow control, improved techniques to control the degree of oxidation are recommended.
- The dual mechanism identified for the oxidation reaction of ilmenite is likely occurring in parallel at and around the transition phase of the reaction. A model applying the two mechanisms in parallel and a assigning an adaptive weight factor to each mechanism would likely more accurately represent the oxidation kinetics.
- A pressure dependent term in the oxidation kinetic model will also prove to be beneficial to run case studies varying the operating pressure and assessing the reactor performance more accurately. To obtain a pressure dependent term in the kinetic model, further experiments are required with varying operating pressure with a constant partial pressure.

- In the present study, the amount of sample used in each test was insufficient for quantitative XRD analysis. To identify the Fe-Ti species present in the crystalline phase, further tests are recommended to generate sufficient sample for quantitative XRD analysis. Fixed bed tests or multiple TGA tests under the same conditions are an option. This would further confirm the phase changes occurring during redox cycles at lower temperatures.
- Further development on the hydrodynamics are required for air reactor modelling and design. The hydrodynamics within the fluidized bed air reactor must be confirmed with CFD modelling and/or experimental data from a cold flow unit. An energy balance must also be added to the reactor model to determine the amount of heat removal necessary for isothermal operation.

References:

[1] Holly Shaftel, R. Jackson, and L. Tenenbaum, “Global Climate Change-Vital Signs of the Planet.” [Online]. Available: https://climate.nasa.gov/vital-signs/global-temperature/. [Accessed: 29-Aug-2017].

[2] H. Gitay, A. Suárez, and R. Watson, “Climate change and biodiversity IPCC,” *IPCC Rep.*, vol. 24, p. 77, 2002.

[3] IEA, “Energy and Climate Change,” *World Energy Outlook Spec. Rep.*, pp. 1–200, 2015.

[4] Aberdeenshire Council, “Canada’s Second Biennial Report on Climate Change,” p. 34, 2016.

[5] IEA, “Key World Energy Statistics 2016,” *Statistics (Ber).*, p. 80, 2016.

[6] IEA, “CO2 emissions from fuel combustion,” *Oecd/Iea*, pp. 1–155, 2016.

[7] P. Sharman, “Cleaner Fossil Power Generation in the 21 st Century - Moving Forwards” UK power Generation Technology Forum, August, 2011.

[8] A. Abad, P. Gayan, L. F. de Diego, F. Garcia-Labiano, and J. Adanez, “Fuel reactor modelling in chemical-looping combustion of coal: 1. model formulation,” *Chem. Eng. Sci.*, vol. 87, pp. 277–293, 2013.

[9] P. Fennell, *1 – Calcium and chemical looping technology: An introduction*. Elsevier, 2015.

[10] F. Zerobin, S. Penthor, O. Bertsch, and T. Pröll, “Fluidized bed reactor design study for pressurized chemical looping combustion of natural gas,” *Powder Technol.*, vol. 316, pp. 569–577, 2017.

[11] CO2 Capture Project (CCP), *CCS Technology Development and Demonstration Results*, vol. 4. 2015.

[12] M. M. Hossain and H. I. de Lasa, “Chemical-looping combustion (CLC) for inherent CO2 separations-a review,” *Chem. Eng. Sci.*, vol. 63, no. 18, pp. 4433–4451, 2008.

[13] P. Cho, T. Mattisson, and A. Lyngfelt, “Comparison of iron-, nickel-, copper- and manganese-based oxygen carriers for chemical-looping combustion,” *Fuel*, vol. 83, no. 9, pp. 1215–1225, 2004.

[14] U.S. Geological Survey, “Titanium mineral concentrates,” *Miner. Commod. Summ.*, vol. 1, no. 703, pp. 172–173, 2012.

[15] L. Qin *et al.*, “Nanostructure formation mechanism and ion diffusion in iron–titanium composite materials with chemical looping redox reactions,” *J. Mater. Chem. A*, vol. 3, no. 21, pp. 11302–11312, 2015.

[16] P. Hallberg, H. Leion, and A. Lyngfelt, “A method for determination of reaction enthalpy of oxygen carriers for chemical looping combustion - Application to ilmenite,” *Thermochim. Acta*, vol. 524, no. 1–2, pp. 62–67, 2011.

[17] J. Adánez, A. Cuadrat, A. Abad, P. Gayán, L. F. D. Diego, and F. García-Labiano, “Ilmenite activation during consecutive redox cycles in chemical-looping combustion,” *Energy and Fuels*, vol. 24, no. 2, pp. 1402–1413, 2010.

[18] P. Perreault and G. S. Patience, “Ilmenite-CO reduction kinetics,” *Fuel*, vol. 165, pp. 166–172, 2016.

[19] C. Linderholm, A. Cuadrat, and A. Lyngfelt, “Energy Procedia Chemical-looping combustion of solid fuels in a 10 kW th pilot – batch tests with five fuels,” *Energy Procedia*, vol. 4, pp. 385–392, 2011.

[20] T. Proll *et al.*, “Natural minerals as oxygen carriers for chemical looping combustion in a dual circulating fluidized bed system,” *Energy Procedia*, vol. 1, no. 1, pp. 27–34, 2009.

[21] J. Ströhle, M. Orth, and B. Epple, “Design and operation of a 1 MWth chemical looping plant,” *Appl. Energy*, vol. 113, pp. 1490–1495, 2014.

[22] J. Strohle, M. Orth, and B. Epple, “Chemical looping combustion of hard coal in a 1 MWth pilot plant using ilmenite as oxygen carrier,” *Appl. Energy*, vol. 157, pp. 288–294, 2015.

[23] A. Cuadrat, A. Abad, P. Gayán, and L. F. De Diego, “The use of ilmenite as oxygen-carrier in a 500 W th Chemical Looping Coal Combustion unit,” vol. 5, pp. 1630–1642, 2011.

[24] P. Moldenhauer, “Testing of minerals and industrial by-products as oxygen carriers for chemical-looping combustion in a 300W test reactor,” *Dep. Energy Environ.*, vol. MSc, 2009.

[25] Y. Tan, F. N. Ridha, M. A. Duchesne, D. Y. Lu, and R. W. Hughes, “Reduction Kinetics of Ilmenite Ore as an Oxygen Carrier for Pressurized Chemical Looping Combustion of Methane,” *Energy & Fuels*, p. acs.energyfuels.7b01038, 2017.

[26] X. Lu *et al.*, “Pressurized chemical looping combustion with CO: Reduction reactivity and oxygen-transport capacity of ilmenite ore,” *Appl. Energy*, vol. 184, pp. 132–139, 2016.

[27] F. García-Labiano, J. Adánez, L. F. de Diego, P. Gayán, and A. Abad, “Effect of pressure on the behavior of copper-, iron-, and nickel-based oxygen carriers for chemical-looping combustion,” *Energy and Fuels*, 2006.

[28] O. Nordness, L. Han, Z. Zhou, and G. M. Bollas, “High-Pressure Chemical-Looping of Methane and Synthesis Gas with Ni and Cu Oxygen Carriers,” *Energy and Fuels*, vol. 30, no. 1, pp. 504–514, 2016.

[29] N. Deshpande, A. Majumder, L. Qin, and L. S. Fan, “High-pressure redox behavior of iron-oxide-based oxygen carriers for syngas generation from methane,” *Energy and Fuels*, vol.

29, no. 3, pp. 1469–1478, 2015.

[30] M. Ishida, H. Jin, and T. Okamoto, “A Fundamental Study of a New Kind of Medium Material for Chemical-Looping Combustion,” vol. 624, no. 3, pp. 958–963, 1996.

[31] H. P. Hamers, F. Gallucci, G. Williams, P. D. Cobden, and M. V. S. Annaland, “Reactivity of Oxygen Carriers for Chemical-Looping Combustion in Packed Bed Reactors under Pressurized Conditions,” 2015.

[32] H. P. Hamers, F. Gallucci, G. Williams, and M. V. S. Annaland, “Experimental demonstration of CLC and the pressure effect in packed bed reactors using NiO / CaAl 2 O 4 as oxygen carrier,” *Fuel*, vol. 159, pp. 828–836, 2015.

[33] M. A. San Pio, F. Gallucci, I. Roghair, and M. van Sint Annaland, “Gas-solids kinetics of CuO/Al2O3 as an oxygen carrier for high-pressure chemical looping processes: The influence of the total pressure,” *Int. J. Hydrogen Energy*, vol. 42, no. 17, pp. 12111–12121, 2017.

[34] R. Xiao, L. Chen, C. Saha, S. Zhang, and S. Bhattacharya, “International Journal of Greenhouse Gas Control Pressurized chemical-looping combustion of coal using an iron ore as oxygen carrier in a pilot-scale unit,” *Int. J. Greenh. Gas Control*, vol. 10, pp. 363–373, 2012.

[35] X. Fu, Y. Wang, and F. Wei, “Phase transitions and reaction mechanism of ilmenite oxidation,” in *Metallurgical and Materials Transactions A: Physical Metallurgy and Materials Science*, 2010.

[36] W. Xiao, X. G. Lu, X. L. Zou, X. M. Wei, and W. Z. Ding, “Phase transitions, micro-morphology and its oxidation mechanism in oxidation of ilmenite (FeTiO3) powder,” *Trans. Nonferrous Met. Soc. China (English Ed.*, vol. 23, no. 8, pp. 2439–2445, 2013.

[37] D. Bhogeswara Rao and M. Rigaud, “Kinetics of the oxidation of ilmenite,” *Oxid. Met.*, vol. 9, no. 1, pp. 99–116, 1975.

[38] F. N. Ridha, M. A. Duchesne, X. Lu, D. Y. Lu, D. Filippou, and R. W. Hughes, “Characterization of an ilmenite ore for pressurized chemical looping combustion,” *Appl. Energy*, vol. 163, pp. 323–333, 2016.

[39] R. W. Hughes, D. Y. Lu, and R. T. Symonds, “Improvement of Oxy-FBC Using Oxygen Carriers: Concept and Combustion Performance,” *Energy & Fuels*, p. acs.energyfuels.7b01556, 2017.

[40] A. Khawan and R. D. Flanagan, “Solid-State kinetic Models: Basic and Mathematical Fundamentals,” *J.Phys.Chem.B*, vol. 110, no. 35, pp. 17315–17328, 2006.

[41] “Hancock and Sharp-Method of Comparing Solid-State Kinetic Data.pdf.” .

[42] P. C. Hayes, “Stability criteria for product microstructures formed on gaseous reduction

of solid metal oxides," *Metall. Mater. Trans. B Process Metall. Mater. Process. Sci.*, vol. 41, no. 1, pp. 19–34, 2010.

[43] A. Abad, J. Adanez, A. Cuadrat, F. Garcia-Labiano, P. Gayan, and L. F. de Diego, "Kinetics of redox reactions of ilmenite for chemical-looping combustion," *Chem. Eng. Sci.*, vol. 66, no. 4, pp. 689–702, 2011.

[44] H. Leion, A. Lyngfelt, M. Johansson, E. Jerndal, and T. Mattisson, "Chemical Engineering Research and Design The use of ilmenite as an oxygen carrier in chemical-looping combustion," vol. 6, no. November 2007, pp. 1017–1026, 2008.

[45] H. Leion, A. Lyngfelt, M. Johansson, E. Jerndal, and T. Mattisson, "The use of ilmenite as an oxygen carrier in chemical-looping combustion," *Chem. Eng. Res. Des.*, vol. 86, no. 9, pp. 1017–1026, 2008.

[46] A. Lambert, E. Comte, D. Marti, T. Sozinho, and S. Bertholin, "On the mechanisms of oxygen carrier degradation during multiple CLC cycles," pp. 2–3, 2013.

[47] F. He, W. P. Linak, S. Deng, and F. Li, "Particulate Formation from a Copper Oxide-Based Oxygen Carrier in Chemical Looping Combustion for CO 2 Capture," *Environ. Sci. Technol.*, vol. 51, no. 4, pp. 2482–2490, 2017.

[48] D. G. Jones, "Photomicrographic investigation of the reduction of ilmenite," *Bull. Acad. Sci. USSR Div. Chem. Sci.*, vol. 26, no. 2, pp. 235–245, 1977.

[49] A. I. Lichtenstein, M. I. Katsnelson, V. I. Anisimov, and D. Vollhardt, "Electronic Correlations to Determine the Phase Stability of Iron up to the Melting". Scientific Reports, 4-5585, 2014

[50] J. Adanez, A. Abad, F. Garcia-Labiano, P. Gayan, and L. L. F. De Diego, "Progress in chemical looping combustion and reforming technology," *Prog Energy Combust Sci*, vol. 38, no. 2, pp. 215–82, 2012.

[51] Y. Zhu, K. Mimura, and M. Isshiki, "Oxidation Mechanism of Copper at 623–1073 K " *Mater. Trans.*, vol. 43, no. 9, pp. 2173–2176, 2002.

[52] V. B. Trindade, R. Borin, B. Z. Hanjari, S. Yang, U. Krupp, and H.-J. Christ, "High-Temperature Oxidation of Pure Fe and the Ferritic Steel 2.25Cr1Mo," *Mater. Res.*, vol. 8, no. 4, pp. 365–369, 2005.

[53] Y. Zhange, W. Lv, X. Lv, C. Bai, K. Han, B. Song, "Oxidation Kinetics of Imenite Concentrate Non-Isothermal Thermogravimetric Analysis" *Journal of Iron and Steel Research*, vol. 24-7, 2017.

[54] E. R. Monazam, R. W. Breault, and R. Siriwardane, "Kinetics of magnetite (Fe3O4) oxidation to hematite (Fe2O3) in air for chemical looping combustion," *Ind. Eng. Chem. Res.*, 2014.

[55] L. Zeng, A. Tong, M. Kathe, S. Bayham, and L. S. Fan, “Iron oxide looping for natural gas conversion in a countercurrent moving bed reactor,” *Appl. Energy*, vol. 157, pp. 338–347, 2015.

[56] X. Bi, “Flow regime transitions in gas-solid fluidization and transport,” University of British Columbia, August, 1994.

[57] H. T. Bi, N. Ellis, I. A. Abba, and J. R. Grace, “A state-of-the-art review of gas–solid turbulent fluidization,” *Chem. Eng. Sci.*, vol. 55, no. 21, pp. 4789–4825, 2000.

[58] D. Kunii and O. Levenspiel, “Circulating fluidized-bed reactors,” *Chem. Eng. Sci.*, vol. 52, no. 15, pp. 2471–2482, 1997.

[59] D. Kunii and O. Levenspiel, “The K-L reactor model for circulating fluidized beds,” *Chem. Eng. Sci.*, vol. 55, no. 20, pp. 4563–4570, 2000.

[60] L. Shampine, J. Kierzenka, and M. Reichelt, “Solving boundary value problems for ordinary differential equations in MATLAB with bvp4c,” *Tutor. Notes*, vol. 75275, pp. 1–27, 2000.

Appendices:

A1. Calculations:

1) Calculation of calcined ilmenite ore composition based on XRD and XRF analysis:

1.1) Determination of elemental composition in crystalline phase:

Table A-1: XRD Results of calcined ilmenite

Component	Mass Fraction (wt%)
Pseudobrookite (Fe_2TiO_5)	46.6
Hematite (Fe_2O_3)	27.0
Rutile (TiO_2)	4.0
Crystallinity	77.5

The composition in the crystalline phase is obtained by normalizing to the crystalline fraction of the compound. The composition in the crystalline phase is: 60.1wt% Fe_2TiO_5, 5.1 wt% TiO_2 and 34.8 wt% Fe_2O_3.

To obtain the elemental composition, the following equations were used:

$$x_{Fe} = Mm_{Fe}(2 * \frac{x_{Fe_2TiO_5}}{Mm_{Fe_2TiO_5}} + 2 * \frac{x_{Fe_2O_3}}{Mm_{Fe_2O_3}})$$

$$x_{Ti} = Mm_{Ti}(\frac{x_{Fe_2TiO_5}}{Mm_{Fe_2TiO_5}} + \frac{x_{TiO_2}}{Mm_{TiO_2}})$$

$$x_O = Mm_O(5 * \frac{x_{Fe_2TiO_5}}{Mm_{Fe_2TiO_5}} + 2 * \frac{x_{TiO_2}}{Mm_{TiO_2}} + 3 * \frac{x_{Fe_2O_3}}{Mm_{Fe_2O_3}})$$

The elemental composition in the crystalline phase is: 52.3 wt% **Fe**, 15.1wt% **Ti**, 32.6 wt% **O**

1.2) Determination of overall elemental composition

Table A-2: XRF Results of calcined ilmenite

Component	Mass Fraction (wt%)
Hematite (Fe_2O_3)	60.9
Rutile (TiO_2)	36.5
Inert	2.6

In the XRF analysis, the total iron present in the ilmenite ore (in both the crystalline and amorphous phases) is given as Fe_2O_3 and the titanium as TiO_2. Hence only the elemental composition can be determined from XRF. The elemental composition calculated below is that of the reactive portion of the sample. Hence the compositions were normalized to 97.4%, to account for the 2.6% inert present in the amorphous phase.

$$x_{Fe} = Mm_{Fe}(2 * \frac{x_{Fe_2O_3}}{Mm_{Fe_2O_3}})$$

$$x_{Ti} = Mm_{Ti}(\frac{x_{TiO_2}}{Mm_{TiO_2}})$$

$$x_O = Mm_O(2 * \frac{x_{TiO_2}}{Mm_{TiO_2}} + 3 * \frac{x_{Fe_2O_3}}{Mm_{Fe_2O_3}})$$

The total elemental composition in reactive portion of the sample is: 43.7 wt% Fe, 22.5 wt% Ti, 33.8 wt% O.

1.3) Determination of elemental composition in the amorphous phase:

$$x_{i,AM} = \frac{x_i - 100 * y_{CR} * x_{i,CR}}{100 * y_{AM}}$$

Where i is the elemental species, AM represents the amorphous phase, CR represents the crystalline phase and y represents the mass fraction in the crystalline or amorphous phase. The elemental composition in the amorphous phase is: 14.0 wt% Fe, 47.9 wt% Ti, 38.1 wt% O.

1.4) Determination of the composition of each component in the amorphous phase:
The ratio of Fe_2TiO_5 to Fe_2O_3 was assumed to be the same as that in the crystalline phase, which is 1.7:1, hence the iron was distributed according to these ratios. The remainder of titanium was assumed to be present as TiO_2. Goal seek was used to determine the composition of each species in the amorphous phase given the elemental composition of the amorphous phase. The composition of the amorphous phase was determined to be: 9 wt% Fe_2O_3, 16.6 wt% Fe_2TiO_5 and 74.4 wt% TiO_2.

1.5) Overall composition of Calcined Ore:
The overall composition is determined by the following equation:

$$x_i = 100 * y_{CR} * x_{i,CR} + 100 * y_{AM} * x_{i,AM}$$

where i represents the component. The inert was assumed to be all in the amorphous phase. The composition of the calcined ore is show in the table below:

Table A-3: Calculated composition of calcined ilmenite

Component	Mass Fraction (wt%)
Pseudobrookite (Fe_2TiO_5)	49.9
Hematite (Fe_2O_3)	28.7
Rutile (TiO_2)	18.8
Inert	2.6

A2. Data Manipulation:

The raw data curve obtained from the pressurized TGA is shown in Figure A-1. Data recording begins upon starting the furnace. Approximately 60 minutes are required to heat and stabilize the TGA to a temperature of 900 ^oC, after which the redox cycles commence. Each oxidation and reduction cycle is followed by a nitrogen purge cycle. Due to high pressure operation, as well as frequent switches between gases of different densities (CO_2 vs. N_2), the raw data curve exhibits mass changes when there should be none, e.g. during the nitrogen purge cycle. For this reason, a blank test is done for each experimental test condition to obtain a baseline curve to subtract from the raw data curve. This is done to remove the effect of buoyancy, gas switches and other effects which cause the baseline drifts. Figure A-2 shows the corrected TGA curve along with the respective raw data and baseline curves for 10^{th} cycle oxidation. The 10^{th} cycle data is used to overcome the activation period noted during the initial redox cycles of ilmenite.

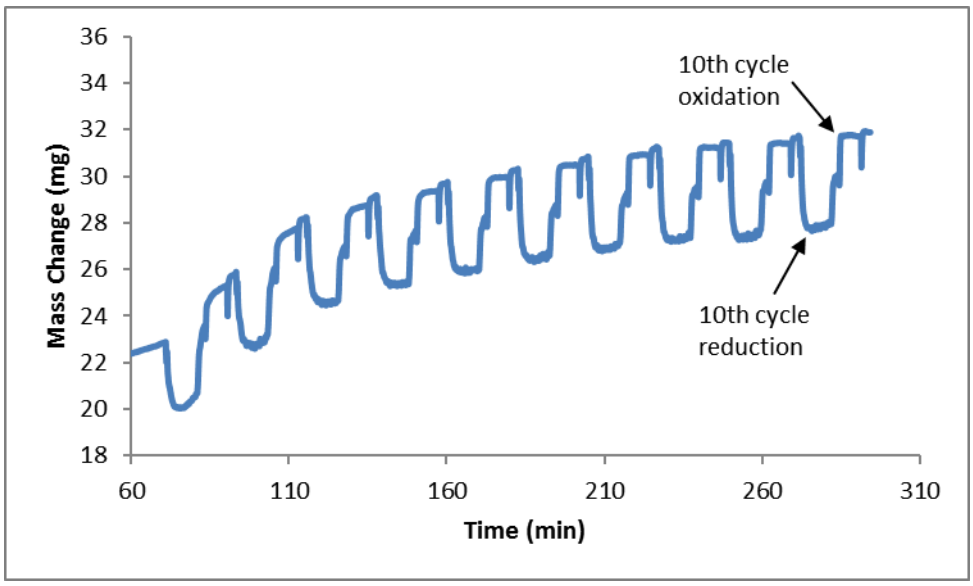

Figure A-1: Raw TGA data curve for 8 bar, 900 °C oxidation in Air

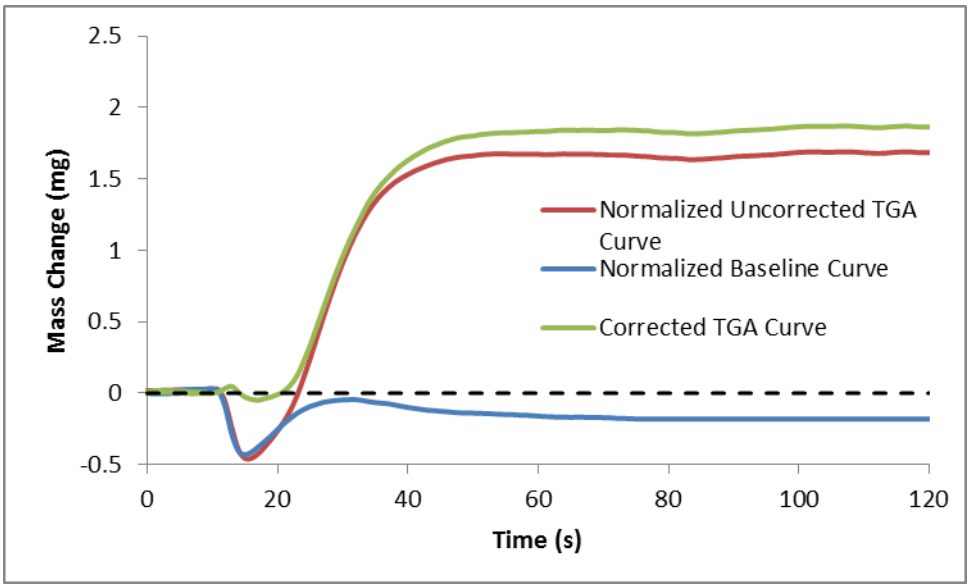

Figure A-2: 10th cycle Baseline, Corrected and Uncorrected TGA curves for 8 bar, 900 °C oxidation in Air

The data was normalized to a carrying capacity of 4.3%. Equation 6 was used to calculate the conversion. Although the data was corrected, dX/dt or IROC curves were used to determine the starting point for the reaction, as shown in Figure 3-1. The instantaneous rate curves are unbiased to the starting point of the reaction, and also offer a better representation of the kinetics.

A3. Preliminary Tests to Determine Operating Conditions:

As the oxidation reaction is relatively fast, the observed reaction rate is likelier to be impacted by external mass transfer limitations. To eliminate the effect of gas film diffusion or inter-particle gas diffusion on the observed kinetics, and ensure the kinetic data obtained from the TGA was intrinsic to the oxidation reaction, preliminary tests were conducted with varying gas flow rate and sample size. A higher gas velocity and smaller sample size are preferred in minimizing external mass transfer limitation. The gas flowrate was increased from 1 NL/min to 3 NL/min, and the sample size decreased from 100 mg to 20 mg.

Figure A-3 shows the TGA kinetics for tests with variable sample size. The oxidation reaction rate continues to increase with a decrease in sample size over the range tested. Ideally a monolayer of particle on the sample pan should be used. However since the mass change from the redox reaction of ilmenite is only about 4.3%, a sufficiently large amount of sample is required to obtain discernible kinetic curves from the TGA. Although the resolution of the TGA balance is 0.5 ug, the effect of background noise on the TGA curves is significant, and is amplified with smaller overall mass changes. Hence a sample size of 40 mg was chosen for the experiments. The difference between the rates of the 43 and 22 mg tests are minor. An image of the sample pan with 40 mg of ilmenite is shown in Figure A-5.

The gas flowrate in the range tested had no effect on the kinetics, as seen in Figure A-4, hence a gas flowrate of 2 NL/min was chosen. The gas flowrate was also chosen to allow for flexibility in changing the flowrate in proportion to changes in the operating pressure, as the gas velocity was to be kept constant. Since the preliminary tests were done at 8 bar, a flowrate of 2 NL/min allowed for higher and lower pressures to be tested maintaining a constant velocity with the given set-up.

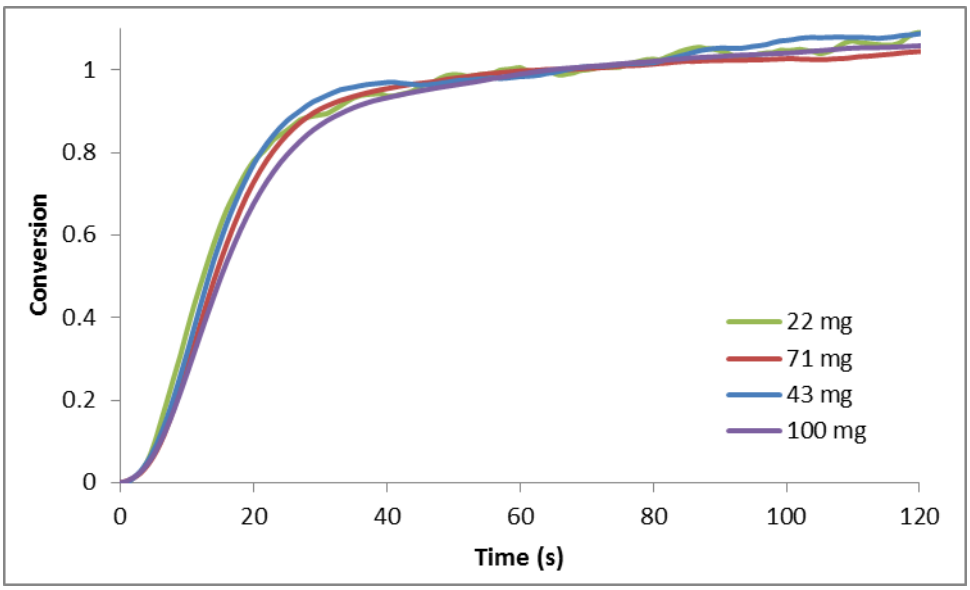

Figure A-3: Effect of Sample Loading on observed oxidation kinetics in Air at 1 NL/min, 8 bar and 900 °C

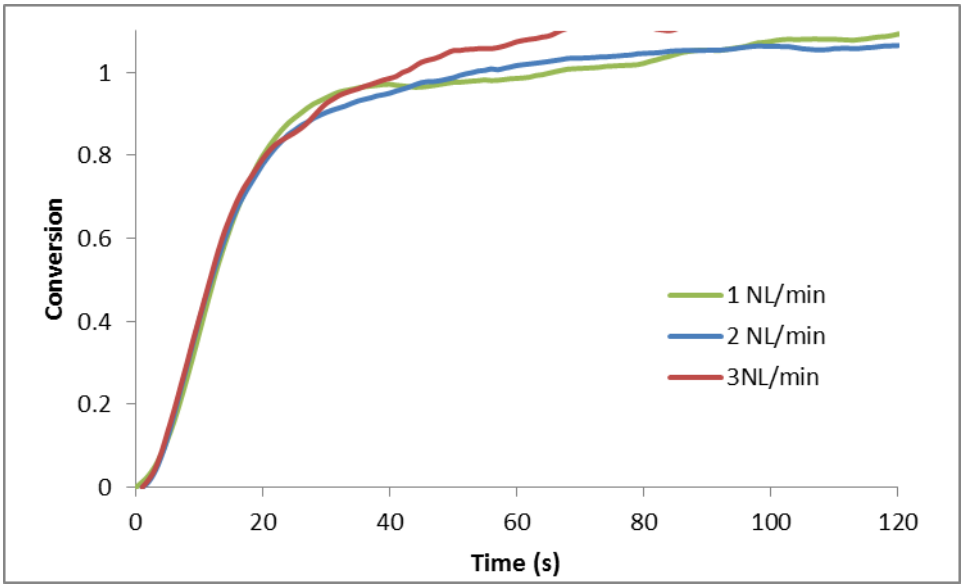

Figure A-4: Effect of flow rate on observed oxidation kinetics with 40 mg sample in Air at 8 bar and 900 °C

Figure A-5: Sample pan loaded with 40 mg of ilmenite sample